



# 1 **Assessing evapotranspiration dynamics across central Europe in the** 2 **context of land-atmosphere drivers**

3 Anke Fluhrer<sup>1,2</sup>, Martin J. Baur<sup>3</sup>, María Piles<sup>4</sup>, Bagher Bayat<sup>5</sup>, Mehdi Rahmati<sup>5</sup>, David Chaparro<sup>1,6</sup>,  
4 Clémence Dubois<sup>7,8</sup>, Florian M. Hellwig<sup>1,7</sup>, Carsten Montzka<sup>5</sup>, Angelika Kübert<sup>9</sup>, Marlin M. Mueller<sup>7,8</sup>,  
5 Isabel Augscheller<sup>1</sup>, Francois Jonard<sup>10</sup>, Konstantin Schellenberg<sup>7,11</sup>, Thomas Jagdhuber<sup>1,2</sup>

6 1 Microwaves and Radar Institute (HR), German Aerospace Center (DLR), Wessling, Germany

7 2 Institute of Geography, University of Augsburg, Augsburg, Germany

8 3 Department of Geography, Cambridge University, Cambridge, UK

9 4 Image Processing Laboratory, University of Valencia, Valencia, Spain

10 5 Institute of Bio-and Geosciences: Agrosphere (IBG-3), Forschungszentrum Jülich, Jülich, Germany

11 6 Centre for Ecological Research and Forestry Applications (CREAF), Cerdanyola del Vallès, Spain.

12 7 Department for Earth Observation, Friedrich Schiller University Jena, Jena, Germany

13 8 Institute of Data Science (DW), German Aerospace Center (DLR), Jena, Germany

14 9 Institute for Atmospheric and Earth System Research (INAR)/Physics, University of Helsinki, Helsinki, Finland

15 10 Earth Observation and Ecosystem Modelling Laboratory, University of Liège, Liège, Belgium

16 11 Department of Biogeochemical Processes, Max-Planck Institute for Biogeochemistry, Jena, Germany

17 *Correspondence to:* Anke Fluhrer ([Anke.Fluhrer@dlr.de](mailto:Anke.Fluhrer@dlr.de))

18 *Keywords:* ICOS, Eddy-covariance, MODIS, SEVIRI, ERA5-land, GLDAS-2, GLEAM, soil moisture, vapor pressure deficit,  
19 extended triple collocation, error cross-correlation, anomaly, binning

## 20 **Abstract.**

21 Evapotranspiration (ET) is an important variable for analysing ecosystems, biophysical processes, and drought-related changes  
22 in the soil-plant-atmosphere system. In this study, we evaluated freely available ET products from satellite remote sensing  
23 (i.e., MODIS, SEVIRI, and GLEAM) as well as modelling and reanalysis (i.e., ERA5-land and GLDAS-2) together with in-  
24 situ observations at eight Integrated Carbon Observation System (ICOS) stations across central Europe between 2017 and  
25 2020. The land cover at the selected ICOS stations ranged from deciduous broad-leaved, evergreen needle-leaved, and mixed  
26 forests to agriculture. Trends in ET were analysed together with soil moisture (SM) and water vapor pressure deficit (VPD)  
27 during four years including a severe summer drought in 2018, but contrasting wet conditions in 2017. The analyses revealed  
28 the increased atmospheric aridity and decreased water supply for plant transpiration under drought conditions, showing that  
29 ET was generally lower and VPD higher in 2018 compared to 2017. Across the study period, results indicate that during  
30 moisture limited drought years, ET is strongly decreasing due to decreasing SM and increasing VPD. However, during normal  
31 or rather wet years, when SM is not limited, ET is mainly controlled by VPD, and hence, the atmospheric demand.  
32 The comparison of the different ET products based on time series, statistics, and extended triple collocation (ETC) shows in  
33 general a good agreement with ETC correlations between 0.39 and 0.99 as well as root-mean-square errors lower than 1.07



34 mm/day. The greatest deviations are found at the agricultural-managed sites Selhausen (Germany) and Bilos (France), with  
35 the former also showing the highest potential dependencies (error cross-correlation) between the ET products. Our results  
36 indicate that ET products differ most at stations with spatio-temporal varying land cover conditions (varying crops over  
37 growing periods and between seasons). This complex heterogeneity complicates the estimation of ET, while ET products agree  
38 at evergreen needle-leaved stations with less temporal changes throughout the year and between years. The ET products from  
39 SEVIRI, ERA5-land, and GLEAM performed best when compared to ICOS observations with either lowest errors or highest  
40 correlations.

## 41 **1 Introduction**

42 Land-atmosphere dynamics and interactions are of key importance for understanding exchange processes in the global water,  
43 energy, and carbon cycles (Zhou et al., 2016). For a holistic and well-founded ecosystem survey, the uptake, consumption, and  
44 release of matter and energy need to be monitored. Especially in times of climate change, availability of terrestrial water,  
45 agricultural productivity assuring food security, as well as forest health guaranteeing, for instance, carbon uptake and  
46 biodiversity preservation, are mainly monitored by soil moisture (SM) and water vapor pressure deficit (VPD; as measure for  
47 atmospheric aridity) (Novick et al., 2016; Zhou et al., 2019; Liu et al., 2020). Many studies focus on these two variables when  
48 analysing drought-related terrestrial ecosystem productivity and its spatio-temporal changes (Fu et al., 2022; Zhang et al.,  
49 2021). Since precipitation (P) ‘and evaporation are the two key components of the global water cycle’ (Miralles et al., 2011),  
50 another important proxy for analysing water stress and its effects on ecosystems is evapotranspiration (ET). As the sum of  
51 evaporation from land, vegetation and water surfaces as well as transpiration from vegetation, ET directly links the terrestrial  
52 energy, water, and carbon cycles (Zhang et al., 2016; Zhou et al., 2016),

53 and integrates meteorological conditions along SM (Bayat et al., 2022). Hence, ET is an important variable for quantifying  
54 biophysical processes, ecosystem functioning, land surface energy and water budgets, as well as improving weather and  
55 climate model predictions (Bayat et al., 2024; Zhang et al., 2016; Zhou et al., 2016). For example, Zhou et al., (2019) reported  
56 negative SM-VPD coupling, meaning low SM and high VPD, due to land-atmosphere feedbacks, since high VPD stimulates  
57 ET, which reduces SM. Although there is a debate that ET alone does not determine SM, and other factors such as precipitation  
58 should also be considered, as reduced P for constant ET can lead to lower SM (Rahmati et al., 2023), ET should in any case  
59 be one of the essential variables to inform about ecosystem-atmosphere dynamics and interactions along with SM and VPD  
60 (Bayat et al., 2021).

61 ET is controlled by biological (e.g., plant growth and plant stomatal regulation) and physical (e.g., temperature) processes. For  
62 example, vegetation controls interannual changes and affects spatio-temporal patterns and trends in ET (Zhang et al., 2016).  
63 ET can be theoretically linked to the independent physical control factors demand (humidity, temperature) and supply  
64 (precipitation). Depending on environmental and meteorological conditions, ET is primarily influenced by one of these three  
65 factors. For instance, across central Europe, ET is mainly driven by the available energy due to reduced solar radiation during



66 cloudy skies (Zhang et al., 2016). However, Seneviratne et al., (2010) stated that decreasing SM leads to decreasing ET due to  
67 the less accessible SM for plant water uptake and increasing soil suction.

68 During summer 2018, Europe experienced an unprecedented drought event comparable to previous extreme droughts, such as  
69 in 2003 and 2010, with a temperature anomaly of +2.8 K (Rakovec et al., 2022) and an abnormally reduced SM and increased  
70 VPD (Fu et al., 2022). This extreme drought was characterized by a unique geographical distribution, focused on regions at  
71 higher latitudes (central and northern Europe), a rapid change from a wet spring to a dry summer, and an intense heatwave in  
72 the spring of 2018 (Bastos et al., 2020). As a result, it caused severe tree stress in central Europe, with low leaf water potential,  
73 leaf discolouration, and premature shedding, leading to significant tree mortality and heavy drought-legacy effects in 2019,  
74 leaving trees vulnerable to further damage from pests and pathogens (Schuldt et al., 2020).

75 The significance of ET can also be seen in relation to the precise parametrization of SM and its memory in Land Surface  
76 Models (LSMs) (Rahmati et al., 2024). Due to its importance and influence on the entire soil-plant-atmosphere system (SPAS),  
77 tracking ET in time and space, meaning at seasonal to multi-year scales and for wide areas, is necessary and calls for a satellite  
78 remote sensing approach (complementary to current modelling and reanalysis approaches). Although it is not directly  
79 measurable from remote sensing acquisitions, optical, thermal, infrared, or microwave observations are used to derive ET  
80 based on surface energy balance, physical and empirical models (Bayat et al., 2021, 2024; Rahmati et al., 2020; Zhang et al.,  
81 2016). Still, research comparing the performance of remote sensing with model and reanalysis data under drought conditions  
82 is lacking, and an analysis on how main ET drivers (SM and VPD) impact these ET products is also needed. Bridging this gap  
83 is paramount to assess which products and in which conditions are more suitable to track ET, especially under the increasingly  
84 frequency and severity of droughts due to climate change.

85 Several sub-global studies exist for comparing various ET products, e.g., over China (Meng et al., 2024; Xu et al., 2024),  
86 across the U.S. (Carter et al., 2018; Xu et al., 2019), over Africa (Trambauer et al., 2014), and across Europe (Ahmed et al.,  
87 2020; Stisen et al., 2021). However, due to the complexity of ecosystems, findings from specific regions (e.g., China, U.S.,  
88 Africa) cannot be generalized for other regions (e.g., Europe). Further, European studies focused either only on spatial product  
89 comparisons, evaluating the performance of hydrological models (e.g., Stisen et al., 2021), on former time periods (e.g., 2003-  
90 2013) at basin scale (Liu et al., 2023), on analysing drought impacts on ET dynamics using solely a single ET product (e.g.,  
91 Sepulcre-Canto et al., 2014; Ahmed et al., 2020), and on evaluating new ET products (e.g., Hu et al., 2023). For example, the  
92 focus in the study of Stisen et al., was the evaluation of the spatial pattern performance in different hydrological models for  
93 ET estimation. For this, four remote sensing based ET products were compared among each other between 2002-2014, and  
94 they found high agreements in spatial patterns across continental Europe (Stisen et al., 2021). Further, Ahmed et al.,  
95 investigated the drought impact of 2018 on the MODerate Resolution Imaging Spectroradiometer (MODIS) ET across  
96 European ecosystems and found that ET decreased up to 50% compared to a 10-year reference period, with agricultural areas  
97 and mixed natural vegetation being most affected (Ahmed et al., 2020). However, there is a lack of studies comparing various  
98 ET products among each other and with in-situ measurements across central Europe, especially during severe drought years  
99 (e.g., 2018), as well as evaluating the potential of remote sensing for tracking seasonal ET dynamics. But the evaluation of the



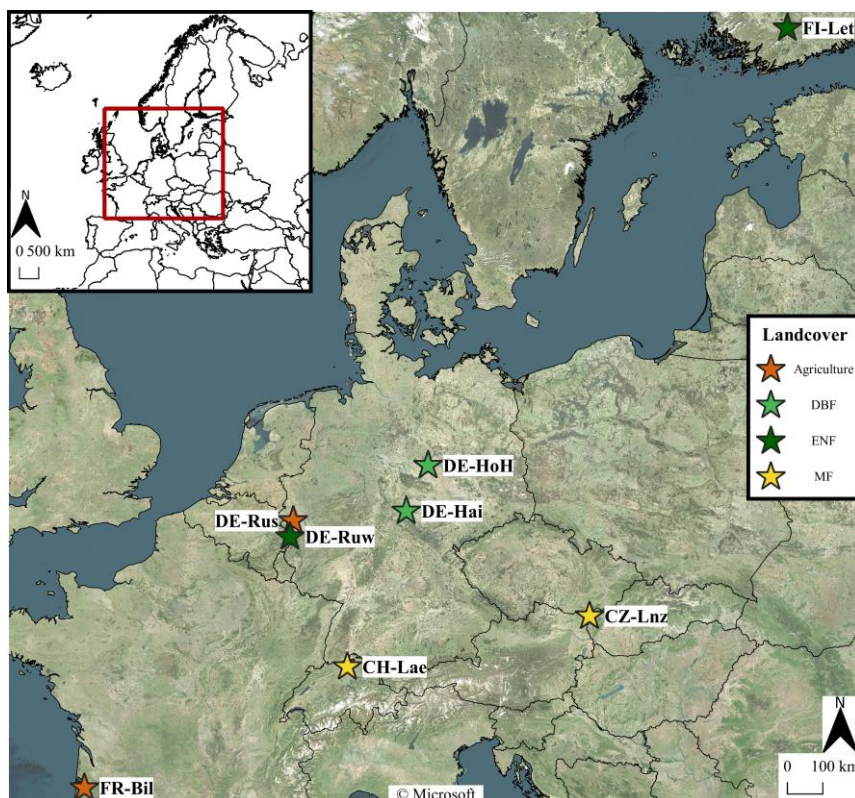
100 varying employed retrieval techniques (e.g., eddy covariance, land surface schemes, Penman-Monteith equation) of commonly  
101 used ET products and how well these techniques perform under drought conditions is paramount in order to capture ET  
102 dynamics correctly.

103 In this study, we first compare the most common ET products from field measurements, modelling, and remote sensing across  
104 central Europe for the period 2017 to 2020. The focus hereby is on the evaluation and quality assessment of the individual  
105 products regarding the estimation of absolute ET values and their time-dynamics. Second, we compare ET products in the  
106 context of SM and VPD, disentangling the relative role of all three variables within the SPAS under severe drought conditions  
107 in 2018 in comparison to the rather wet year 2017. This is to analyse how the ET products catch drought conditions and to  
108 what extent they can be used as indicator for drought events.

## 109 2 Materials and Methods

### 110 2.1 Study area

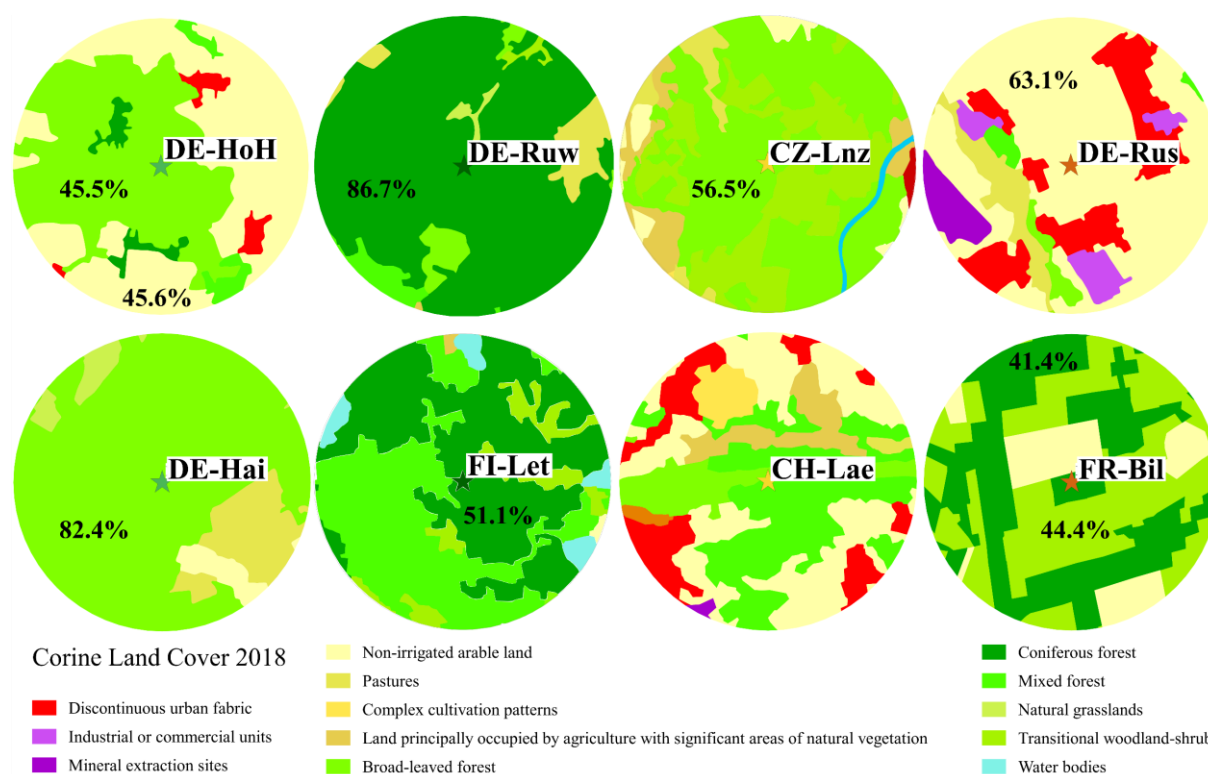
111 The focus is on eight Integrated Carbon Observation System (ICOS) (Rebmann et al., 2018) stations within central Europe  
112 between 2017 and 2020, where field-scale in-situ eddy-covariance (EC) ET measurements are available (see Fig. 1).



113  
114 Figure 1: Location of the eight investigated Integrated Carbon Observation System (ICOS) stations in central Europe, and their classification  
115 according to the respective dominant land cover class. DBF = deciduous broad-leaved, ENF = evergreen needle-leaved, MF = mixed forest.



116 The study comprises two deciduous broad-leaved (DBF) — the German Hohes Holz (DE-HoH) and Hainich (DE-Hai), two  
 117 evergreen needle-leaved (ENF) — the German Wuestebach (DE-Ruw) and Finnish Lettosuo (FI-Let), and two mixed forest  
 118 (MF) stations — the Czech Landzhot (CZ-Lnz) and the Swiss Laegern (CH-Lae), as well as two agriculture stations — the  
 119 German Selhausen (DE-Rus) and the French Bilos (FR-Bil). At every station, a footprint of 3 km radius is analysed to account  
 120 for differences in spatial resolutions among employed datasets (see Sec. 2.2 and Tab. 1). As displayed in Figure 2 and Table  
 121 S1 (supplement), the land cover types and their homogeneity within the 3 km × 3 km footprint around every station was  
 122 analysed based on the Corine land cover (CLC) 2018 classification from the Copernicus Land Monitoring Service at 100 m  
 123 spatial resolution (European Environment Agency, 2019).



124  
 125 Figure 2: Overview of land cover classes according to the Corine Land Cover (CLC) 2018 (European Environment Agency, 2019) within  
 126 the 3 km × 3 km footprint around every investigated ICOS station. Percentages inside the circles indicate the dominant land cover classes,  
 127 respectively. The percentages of all land cover classes at every station can be found in the supplement (see Tab. S1).

128 According to this classification, two stations can be considered as homogeneous with one dominant land cover class, i.e., 86.7  
 129 % of coniferous forest at DE-Ruw, and 82.4 % of broad-leaved forest at DE-Hai. Station DE-Rus is mainly (63.1 %) covered  
 130 by non-irrigated arable land. Further, two stations show a two-part split land cover with two almost equally dominant classes.  
 131 At DE-HoH, 45.6 % are covered by non-irrigated arable land and 45.5 % are covered by broad-leaved forest. At FR-Bil,  
 132 although it is officially labelled as ENF station, 44.4 % are covered by transitional woodland shrub, while 41.4 % are covered  
 133 by coniferous forest, a managed Pine forest plantation (Loustau et al., 2022). Hence, due to this heterogeneity and the fact that

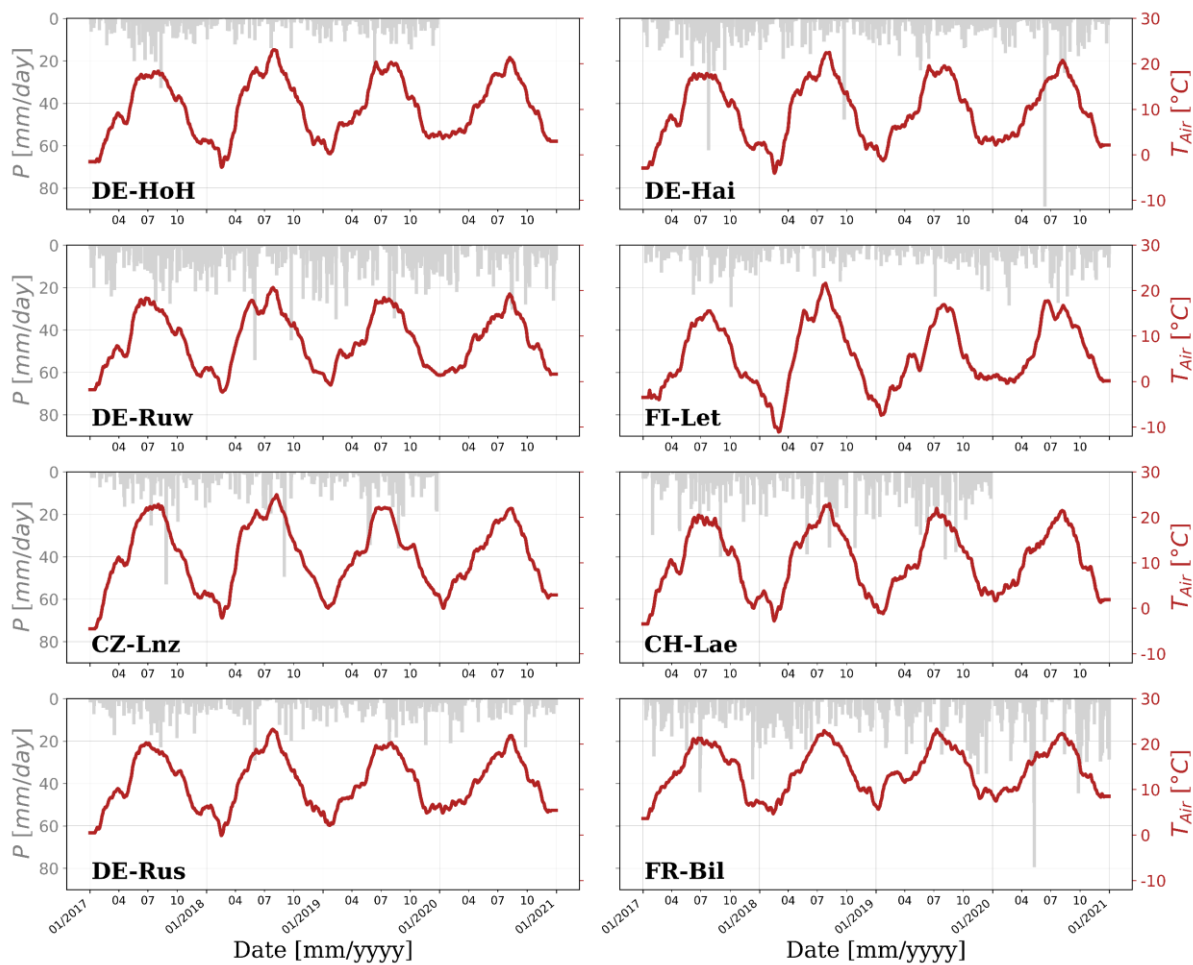




134 14.2 % of non-irrigated arable land (see Tab. S1) are mostly directly located near the station (see Fig. 2), we ranked it as  
135 agricultural station in order to account for the frequently changing land cover conditions and spatial heterogeneity. All other  
136 stations are rather heterogeneous with a mix of more than two different land cover classes (see Tab. S1 and Fig. 2). However,  
137 it is worth noting that the CLC 2018 classification is based on data from 2017 to 2018. Hence, changes in the land cover, e.g.,  
138 such as differences between summer and winter months, deforestation, weather extremes (storms, floods), or varying  
139 agricultural crop cultivation, at each station between 2017 to 2020 are not included here.

140 Figure 3 illustrates the meteorological conditions (precipitation  $P$  and air temperature  $T_{\text{Air}}$ ) at every station during the  
141 investigation period. Note that the in-situ  $P$  measurements contain missing values at stations DE-HoH, CZ-Lnz, and CH-Lae  
142 in 2020. The overall lowest  $T_{\text{Air}}$  is found at the northernmost ICOS station FI-Let, varying between  $-12.6$  °C (absolute  
143 minimum) and  $22.75$  °C (absolute maximum) in the years 2017 to 2020, with an interannual average of  $5.67$  °C. In contrast,  
144 the highest average  $T_{\text{Air}}$  (between 2017 and 2020) of  $14.1$  °C is found at the southernmost ICOS station FR-Bil, which also  
145 has the highest average  $P$  value of  $3.04$  mm/day. The lowest  $P$  is found at DE-HoH with an average of  $1.26$  mm/day, which is  
146 similar to the other stations in the mid-latitudes. The overall highest  $T_{\text{Air}}$  and lowest  $P$  at every station are always found in 2018  
147 with an average of  $1.7$ °C higher  $T_{\text{Air}}$  and annual  $0.76$  mm higher  $P$ , compared to the second hottest and driest year in each case.  
148 Exceptions can be found at the station FR-Bil, where the highest  $T_{\text{Air}}$  are recorded in 2019 and lowest  $P$  in 2017, and DE-Ruw,  
149 as well as CH-Lae, where the lowest average annual  $P$  are recorded in 2020, respectively.

150 Based on the standardized precipitation-evapotranspiration index (SPEI) (Beguería et al., 2023) (see Fig. S1), which describes  
151 drought based on the amount and duration of water deficit (Yu et al., 2023), distinctly dry and wet years are identified for each  
152 ICOS station. While all stations show abnormally dry periods, especially for 2018, only stations FI-Let and FR-Bil show  
153 abnormally wet periods at the end of 2017 and 2019. These two are the northernmost and southernmost stations (see Fig. 1).



154

155 Figure 3: Daily in-situ measured precipitation (P) [mm/day] and air temperature ( $T_{Air}$ ) [°C] at investigated ICOS stations.  $T_{Air}$  was cleaned  
156 for daily and weekly dynamics using a Savitzky-Golay (Savitzky and Golay, 1964) filter with a window size of 31 days.

## 157 2.2 Data base

158 In the first part of this study, different ET products (see Tab. 1) are inter-compared in order to evaluate the potential of remote  
159 sensing for tracking seasonal ET dynamics. The in-situ ET data, recorded at the ICOS stations at field-scale, are mass balance-  
160 based measurements of sensible heat (H) and latent heat (LE) fluxes through the covariance of heat and moisture fluxes,  
161 respectively. The LE [ $W/m^2$ ] can then be converted to ET by dividing it by the latent heat of vaporization (2.434 [MJ/kg] at  
162 20 °C air temperature) (Allen et al., 1998). The ICOS network has undertaken a large effort to ensure high-quality LE  
163 measurements, which are comparable among different ICOS stations (Rebmann et al., 2018). Besides in-situ EC ET  
164 measurements, we employ optical/thermal remote sensing products from NASA's (National Aeronautics and Space  
165 Administration) Moderate-resolution Imaging Spectroradiometer (MODIS) sensor on Terra (Running et al., 2017), ESA's  
166 Spinning Enhanced Visible and Infrared Imager (SEVIRI) sensor onboard of the Meteosat Second Generation (MSG) satellites,



167 and the Global Land Evaporation Amsterdam Model (GLEAM) (Martens et al., 2017). Further, also reanalysis and modelling  
 168 products from the land component of the Earth system modelling product European Re-Analysis (ERA5-land) from the  
 169 European Centre for Medium-Range Weather Forecasts (ECMWF) (Muñoz Sabater, 2019), and from NASA’s Global Land  
 170 Data Assimilation System Version 2 (GLDAS-2) (Beaudoing, 2019) are used (see Tab. 1). It should be noted that the GLEAM  
 171 product is based on various remote sensing observations and reanalysis datasets from, e.g., NASA’s SMOS (soil moisture and  
 172 ocean salinity) mission, MODIS, GLDAS-Noah, and ERA-Interim (Martens et al., 2017). The MODIS product with nominal  
 173 spatial resolution of 500 m is aggregated to the 3 km footprint, while the SEVIRI, ERA5-land, GLDAS-2, and GLEAM  
 174 products are maintained at their original spatial resolutions of 3 km, 9 km and 25 km, respectively. All datasets are temporally  
 175 aggregated to daily time series.

176 Table 1: Overview of investigated ET products presenting the data source, the original spatial and temporal resolution as well as the retrieval  
 177 basis and method of each product.

| <b>PRODUCT<br/>(NAME)</b>                      | <b>SOURCE</b>   | <b>ORIGINAL<br/>SPATIAL /<br/>TEMPORAL<br/>RESOLUTION</b> | <b>RETRIEVAL<br/>BASIS</b>   | <b>RETRIEVAL<br/>METHOD</b>               |
|--|---|---|------------------------------|---|
| <b>ICOS (Level 2)</b>                          | ICOS (ICOS RI et al., 2024)   | Point scale / Half-hourly                                 | In-situ measurements         | Eddy covariance technique                 |
| <b>MODIS<br/>(MOD16A2)</b>                     | NASA (Running et al., 2017)   | 500m / 8-daily  | Remote Sensing               | Penman-Monteith                           |
| <b>ERA5-land</b>                               | ECMWF (Muñoz Sabater, 2019)   | 9 km / hourly   | Reanalysis                   | ECMWF’s IFS, H-TESSEL land surface scheme |
| <b>SEVIRI<br/>(METv3)</b>                      | ESA (Bayat et al., 2022)  | 3 km / half-hourly  | Remote Sensing               | SVAT, (H-) TESSEL land surface scheme     |
| <b>GLDAS-2<br/>(GLDAS_NOAH<br/>025_3H_2.0)</b> | NASA (Beaudoing, 2019)  | 25 km / 3-hourly  | Land Surface Model (NOAH) L4 | Penman-Monteith                           |
| <b>GLEAM (v3)</b>                              | University of Amsterdam (Miralles et al., 2011; Martens et al., 2017) | 25 km / daily   | Remote Sensing               | Priestley-Taylor                          |

178 In Table 1, the retrieval methods for each ET product are given. MODIS and GLDAS-2 are based on physically-based methods  
 179 employing the Penman-Monteith equation (Penman, 1948; Monteith, 1965), while GLEAM is based on the Priestley-Taylor  
 180 equation (Priestley and Taylor, 1972), and ERA5-land uses the ECMWF integrated forecasting system (IFS) and is derived  
 181 from the ERA5 product where the land surface model is based on the hydrology Tiled ECMWF Surface Scheme for Exchange





182 Processes over Land (H-TESSSEL) (Hersbach et al., 2020). Further, SEVIRI employs a soil-vegetation-atmosphere-transfer  
183 (SVAT) approach also based on the physics of the TESSSEL and H-TESSSEL land surface scheme (Balsamo et al., 2009; Bayat  
184 et al., 2024; Ghilain et al., 2011). The Priestley-Taylor equation does not consider the impact of VPD or canopy conductance  
185 (Wang and Dickinson, 2012), while within the Penman-Monteith equation VPD and relative humidity (RH) are used according  
186 to the function of Fisher et al., (2008) in order to account for soil water stress when calculating the actual soil evaporation.  
187 Further, the canopy conductance is retrieved from stomatal and cuticular conductance depending on LAI and the wet surface  
188 fraction, with the stomatal conductance constrained by VPD and minimum air temperature and the cuticular conductance fixed  
189 to a constant of 0.01 [mm/s] (Running et al., 2019; Wang and Dickinson, 2012). Hence, the Penman-Monteith equation is more  
190 accurate and often outperforms the Priestley-Taylor equation but, in turn, requires more ‘parameters that are difficult to  
191 characterize’ (Fisher et al., 2008). Within the TESSSEL and H-TESSSEL schemes, canopy conductance is formulated according  
192 to the modified Jarvis function and based on the stomatal conductance (retrieved from net assimilation and Kirchhoff’s  
193 resistance/conductance analogy) and cuticular conductance (fixed between 0 to 0.25 [mm/s] according to vegetation types),  
194 while SM at four layers, and therefore also deeper soil layers, are accounted when defining the soil water stress on soil  
195 evaporation (ECMWF, 2018). Lastly, for this study, it is interesting to note that GLEAM and ERA5-land employ the ECMWF  
196 atmospheric reanalysis data (Li et al., 2022), while GLDAS-2 is based on MODIS land surface parameters (Rui and Beaudoin,  
197 2022). These product interdependencies should be kept in mind during interpretation of results.

198 In the second part of this study, the ET products are compared in relation to two dominant parameters of the SPAS, namely  
199 SM and VPD. While VPD comes from in-situ measurements of the Fluxnet network (point precise), SM comes from NASA’s  
200 Soil Moisture Active Passive (SMAP) mission, the multi-temporal dual channel algorithm (MT-DCA) L-band (1.4 GHz)  
201 dataset (9 km spatial resolution) (Konings et al., 2016; Feldman et al., 2021). We employed the SMAP SM in this study instead  
202 of using available in-situ measurements of the Fluxnet network, since the latter were of poor quality at several stations and  
203 years, and we wanted to build our analyses on one continuous dataset. The SMAP MT-DCA dataset is quality controlled and  
204 filtered for, e.g., snow, frozen ground, and water bodies (Feldman et al., 2021).

## 205 **2.3 Methods**

### 206 **2.3.1 Extended triple collocation**

207 For the comparison of different ET products in sec. 3.1., the extended triple collocation (ETC) method (McColl et al., 2014)  
208 is employed. The ETC technique not only provides the root-mean-square-error  $\sigma_\epsilon$  [mm/day] of the classical triple collocation  
209 (TC) method (Stoffelen, 1998) among three independent measurement systems, but also provides the correlation  $\rho_{t,X}$  [-] among  
210 them, giving the sensitivity of the measuring systems. The most important advantage of the TC and ETC techniques is that  
211 one can calculate  $\sigma_\epsilon$  and  $\rho_{t,X}$  without considering any of the systems as the necessary reference. The product with the lowest  
212  $\sigma_\epsilon$  and highest  $\rho_{t,X}$  identifies the one with the lowest uncertainty. As input to the ETC, the daily ET time series are filtered for  
213 the growing season (April to October) of each year. With the aim of evaluating the performance of the remote sensing products



214 (SEVIRI, MODIS, GLEAM), we compare them individually with ERA5-land and in-situ measurements (ICOS) on the one  
215 hand, and with GLDAS-2 and ICOS on the other hand. Sanity checks for Gaussian distributions and large sample sizes of  
216 ~853 values per product ensure precise and representative ETC analyses. Additionally, since one of the requirements for  
217 thorough ETC analyses is the independence among evaluated datasets (McColl et al., 2014), the error cross-correlation (ECC)  
218 values (Gruber et al., 2016) are calculated in order to evaluate product dependencies. In case the ECC lies between -0.5 and  
219 0.5, the datasets can be regarded as independent from each other. The ECC for each product comparison (with ET product  $\in$   
220 [i,j,k,l]) is calculated from the error cross covariance  $\sigma_{\varepsilon_i \varepsilon_j}$  between two products as well as the random error variance  $\sigma_{\varepsilon_i}^2$  of  
221 each dataset, respectively (Gruber et al., 2016):

$$222 \quad ECC_{ij} = \frac{\sigma_{\varepsilon_i \varepsilon_j}}{\sigma_{\varepsilon_i}^2 \sigma_{\varepsilon_j}^2}, \quad (1)$$

223 with

$$224 \quad \sigma_{\varepsilon_i \varepsilon_j} = \sigma_{ij} - \frac{\sigma_{ik} \sigma_{jl}}{\sigma_{kl}}, \quad (2)$$

225 and

$$226 \quad \sigma_{\varepsilon_i}^2 = \sigma_i^2 - \frac{\sigma_{ij} \sigma_{ik}}{\sigma_{jk}}. \quad (3)$$

### 227 2.3.2 Anomalies

228 For the comparison of different SPAS parameters in sec. 3.2., the seasonal imprint is removed from the signals in order to  
229 focus on exceptional events in the time series. For that, we calculated the 30-day anomaly time series for each parameter. To  
230 do so, the daily average over all four years was calculated first. The resulting daily average was then smoothed using a  
231 Savitzky-Golay (Savitzky and Golay, 1964) filter with a window size of 61 days. Lastly, for every day between 2017 to 2020,  
232 the difference between the day of interest and the 30-day average of the filtered daily average before that day has been  
233 calculated.

### 234 2.3.3 Binning

235 To analyse the effects of water supply and demand on ET, we binned daily ET values into a grid of 30 by 30 SM and VPD  
236 conditions, with SM ranging between 0.0001 vol.% and 40 vol.%, and VPD ranging between 0.0001 hPa and 25 hPa, both in  
237 31 steps (to create a grid of 30 by 30). While SM is indicative of the available water supply, VPD is an indicator of atmospheric  
238 water demand. The co-regulation of ET by SM and VPD is complex as it depends on stomatal and surface conductance, which  
239 in turn are dependent on SM and VPD, as well as vegetation and soil properties (Carminati and Javaux, 2020; Zhang et al.,  
240 2021; Vargas Zeppetello et al., 2023). To understand the main directionality of ET changes relative to SM, we calculated the

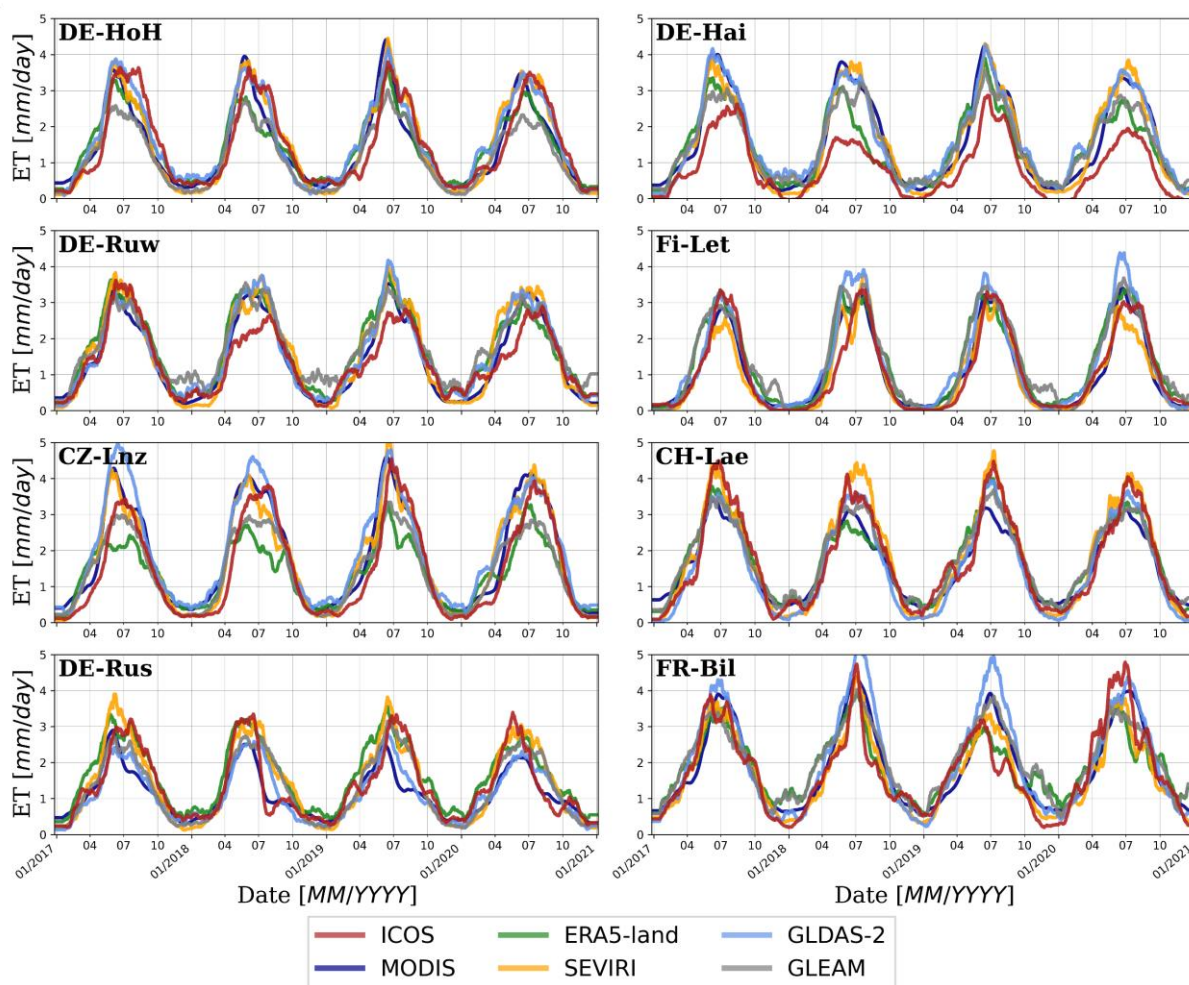


241 average slopes of ET relative to SM (equivalent to  $\frac{\Delta ET}{\Delta SM}$ ). The same applies when we examine the directionality of the ET  
242 changes with respect to VPD ( $\frac{\Delta ET}{\Delta VPD}$ ). These analyses are done in order to get an indication of the dominating control on ET.

### 243 3 Results

#### 244 3.1 Differences in examined ET products

245 In Figure 4, times series of the employed ET products (see Tab. 1) are shown at all investigated ICOS stations (see Fig. 1) for  
246 the period 2017 to 2020. Apart from the seasonal dynamics of ET, with highest values in the summer months (June, July,  
247 August) and low values but with more frequent changes in the winter months (November, December, January), the overall  
248 good consistency between the different ET products can be noted.



249

250 Figure 4: Comparison of seasonal dynamics of ET [mm] products for the period 2017-2020 at investigated ICOS stations. All time series  
251 were cleaned for daily and weekly dynamics using a Savitzky-Golay (Savitzky and Golay, 1964) filter with a window size of 31 days.



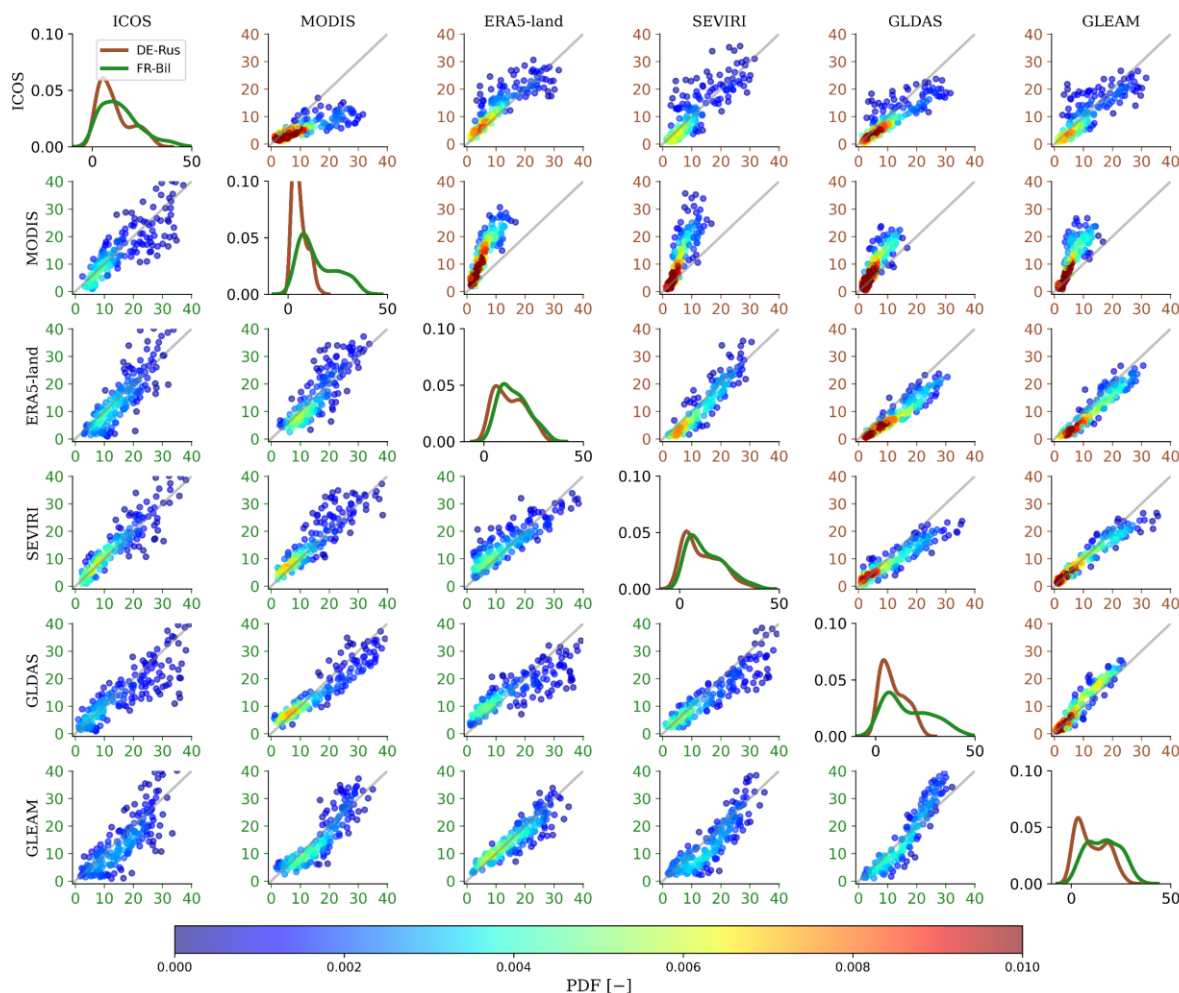
252 The highest variability among products and ET dynamics can be observed during summer months, with greatest differences at  
253 stations DE-Hai and DE-Ruw when comparing all products to the ICOS measurements. Here, the ground-based ET shows  
254 always lower values across all years for DE-Hai, and in 2018 and 2019 for DE-Ruw. Additionally, for each year, the ICOS ET  
255 rises a few weeks later than the other products at both stations but decreases together with all other ET products. At station  
256 CZ-Lnz, ERA5-land shows the overall lowest ET values during the growing period (April to October). Further, the highest ET  
257 values are found at station FR-Bil for the GLDAS-2 product with most pronounced differences to all other products in 2018,  
258 while overall lowest values across all years and ET products are displayed at DE-Rus. At the latter, ET values never exceed 4  
259 mm/day. From this daily time series analyses, the largest differences among ET products can be seen at the DBF station DE-  
260 Hai, MF station CZ-Lnz, and agriculture station DE-Rus. At DE-Hai, the ICOS ET is overestimated by all other products, at  
261 CZ-Lnz, the ERA5-land product is lower compared to all other ET products, especially in the summer months, and at DE-Rus,  
262 the MODIS and often also the ICOS product are overestimated by the ERA5-land and SEVIRI products. Hence, no clear  
263 pattern at all stations and between different land cover classes can be found.

264 For more detailed analyses, daily time series of ET products are averaged to 8-daily sums in order to account for the coarse  
265 temporal resolution of the MODIS product (see Tab. 1). In Figure 5, the 8-daily ET products are compared with each other at  
266 the two agriculture stations. The same illustrations for the forest stations can be found in the supplement (see Figs. S2-S4).  
267 These figures show the scatter plots between ET products giving the probability density function (PDF) of points (by colour)  
268 below (left panels) and above (right panels) the matrix diagonal, as well as the PDF curves for each site and product in the  
269 diagonal of the matrix. They support the previously stated good consistency between ET products but outline the exact  
270 differences on 8-days scale in more detail. The highest density of values can be observed between 0 to 10 mm/8-days at all  
271 stations except at DE-Ruw and FR-Bil. This comes from the rather low ET values during the autumn, winter, and spring  
272 seasons due to the overall reduced solar radiation combined with decreased vegetation cover during cold months. However, at  
273 stations DE-Ruw (see Fig. S3, right panels) and FR-Bil (see Fig. 4, left panels), the density of values is shifted towards higher  
274 ET (0 to 20 mm/8-days). These are two out of the three stations covered by coniferous forest. While FR-Bil has a two-part  
275 split land cover in the footprint (shrub and coniferous forest), DE-Ruw is almost homogeneously covered by coniferous forest  
276 (see Fig. 2), and both stations show higher ET values during autumn and spring seasons compared to all other stations due to,  
277 e.g., the lack of leaf off conditions during that periods. The third station covered by coniferous forest (FI-Let), however, shows  
278 the density of values between 0 to 10 mm/8-days (see Fig. S3, left panels), similar to DBF and MF stations. This is the  
279 northernmost station, typically covered with snow between November and March.

280 Further, the over- or underestimation of values between two products can be seen, such as the overestimation of ICOS  
281 compared to all other ET products at DE-Hai for higher ET values, affirmed by the PDF for ICOS peaking at the highest  
282 density (see Fig. S2, left panels). There is also an overestimation of MODIS compared to all other products at DE-Rus (see  
283 Fig. 5, right panels) and CH-Lae (see Fig. S4, left panels) when ET values are higher. DE-Rus is the only homogeneously  
284 covered agricultural station with potentially most changes in land cover classes during the seasons and years, showing the  
285 greatest differences in ET products due to the overall higher complexity of agricultural plants and more frequent alterations.



286 While the PDF of MODIS at DE-Rus peaks at the highest density and gives the smallest range of ET values across all stations,  
 287 a bimodal distribution of densities is displayed at CH-Lae. This bimodal distribution of densities is also noticeable at other  
 288 products and stations but stronger always for MODIS.



289

290 Figure 5: Comparison of seasonal dynamics of ET [mm/8-days] products for the period 2017-2020 at investigated ICOS stations DE-Rus  
 291 (right panels above the diagonal of the matrix) and FR-Bil (left panels below the diagonal of the matrix). All time series were averaged to 8-  
 292 daily sums at MODIS dates, and cleaned for daily and weekly dynamics using a Savitzky-Golay (Savitzky and Golay, 1964) filter with a  
 293 window size of 31 days.

294 This visual interpretation is also supported by statistics in supplement Figures S5-S7. In general, the highest coefficient of  
 295 determination,  $R^2$  [-], among all products can be found at station CH-Lae, while the overall lowest root-mean square errors,  
 296 RMSE [mm/8-days], are retrieved at both ENF stations (DE-Ruw, FI-Let). DE-Ruw is also the station with, in general, lowest  
 297 percentage bias, PBIAS [%], among all ET products. In detail, the highest  $R^2$  of 0.94 is found between GLEAM and GLDAS-  
 298 2 at CH-Lae, while the lowest RMSE of 2.3 mm/8-days and the lowest PBIAS of -0.05 % is found between GLEAM and

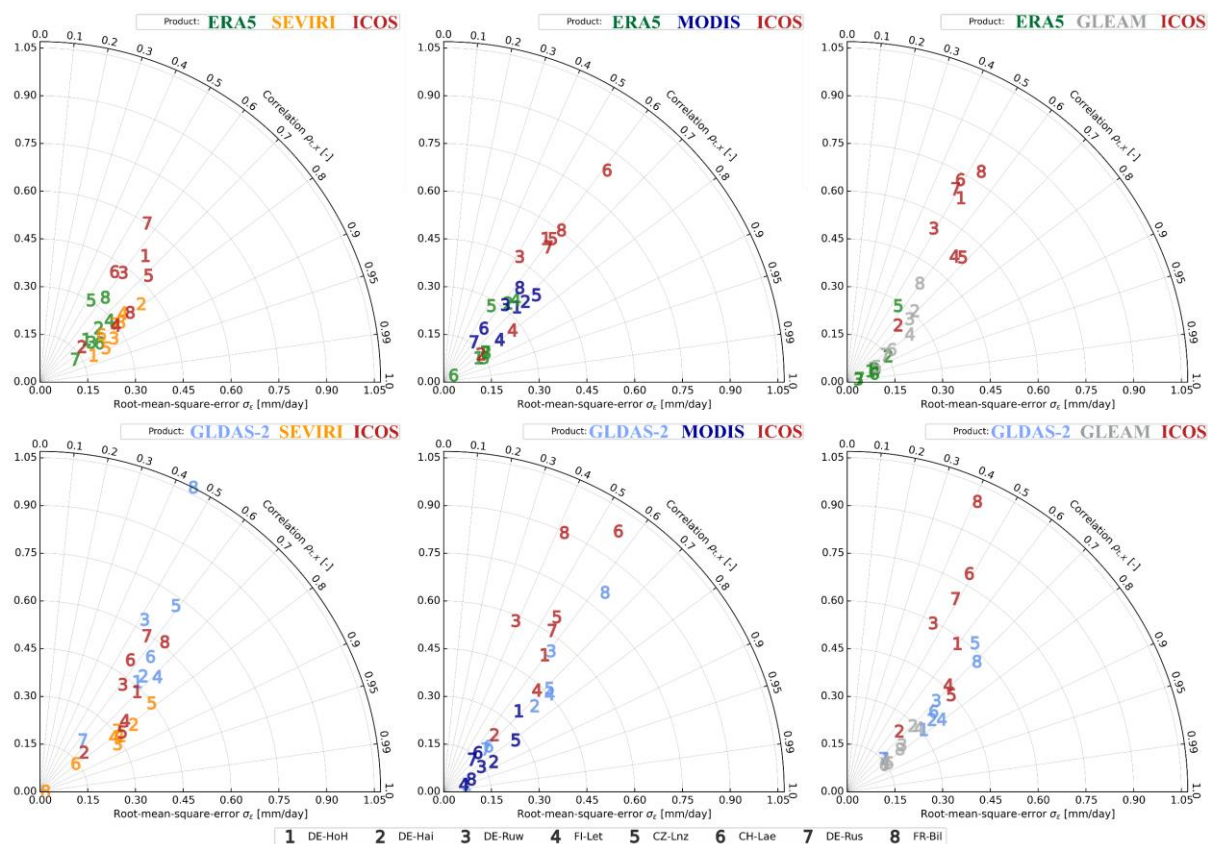




299 ERA5-land again at CH-Lae. The lowest  $R^2$  of 0.62 and highest PBIAS of 91 % is found between ICOS and MODIS at the  
300 agricultural station DE-Rus, while the highest RMSE of 8.8 mm/8-days is found between MODIS and ERA5-land again at  
301 DE-Rus. In summary, the statistics indicate an overall worse consistency among products at the rather mixed agricultural  
302 station (DE-Rus) and better consistency at ENF stations.

303 In order to evaluate the performance of each ET product in more detail, the ETC method (McColl et al., 2014) is employed.  
304 Here, we use the ETC approach to compare the three remote sensing products individually first with ERA5-land and ICOS,  
305 and then with GLDAS-2 and ICOS. The preceding calculation of ECC values among all products (see Fig. S8) is conducted  
306 to ensure the independence of the examined products, which is required by ETC analysis (see Sec. 2.3.1). Overall, ECC values  
307 are always around zero or within the acceptable range of -0.5 to 0.5. Only at station DE-HoH between GLDAS-2 and GLEAM,  
308 at CZ-Lnz between ERA5-land and GLEAM, at CH-Lae between ERA5-land and MODIS as well as for all product  
309 comparisons at DE-Rus (except between ERA5-land and SEVIRI), ECC values outside the acceptable range can be found (see  
310 Fig. S8). The high ECC values at DE-HoH, CZ-Lnz, and DE-Rus between GLEAM and GLDAS-2 or ERA5-land is not  
311 surprising, since the GLEAM product is based on various remote sensing and reanalysis datasets, with among others GLDAS  
312 and ERA5 (see Sec. 2.2). Hence, at most stations ET products can be regarded as statistically independent from each other.  
313 Only some potential product dependencies, especially at the agricultural station DE-Rus, should be kept in mind during the  
314 interpretation of ETC results.

315 In Figure 6, the ETC statistics for the applied product combinations at all stations are shown. While the x- and y- axes represent  
316 the estimated root-mean-square-error  $\sigma_\varepsilon$ , the arcs give the correlation  $\rho_{t,x}$ . Hence, numbers (representing the eight stations)  
317 close to zero on the x- and y-axes and close to one on the arcs give the best ETC results, meaning lowest uncertainty of the ET  
318 product (represented by colours) compared to the other two products, respectively. It can be seen that all  $\sigma_\varepsilon$  values are below  
319 1.07 mm/day due to the overall high consistency among ET products, with correlations between  $0.39 < \rho_{t,x} < 0.99$ . However,  
320 products with highest  $\rho_{t,x}$  necessarily do not have the lowest  $\sigma_\varepsilon$ . Hence, the discrepancy between products varies but does not  
321 dominate differences in the sensitivity among products. The highest  $\sigma_\varepsilon$  is found at station FR-Bil for GLDAS-2, when  
322 comparing GLDAS-2 with GLEAM and ICOS. The lowest  $\rho_{t,x}$  of 0.33 is found at station DE-Ruw for ICOS as the results of  
323 the ETC among GLDAS, MODIS, and ICOS. Despite the high ECC values at DE-Rus (see Fig. S8) and hence, potential  
324 product dependencies, ETC results at this station are inconspicuous with comparable errors and correlations. Overall, ERA5-  
325 land, SEVIRI, and GLEAM perform better at all stations with either lowest errors or highest correlations within their ETC  
326 triplets. In summary, compared to ERA5-land and ICOS, the remote sensing products (SEVIRI, MODIS, GLEAM) show  
327 similar uncertainties as ERA5-land, but at most stations ERA5-land outperforms GLEAM and MODIS (see Fig. 6, upper row).  
328 Further, compared to GLDAS-2 and ICOS, the remote sensing products in most cases outperform GLDAS-2 and ICOS,  
329 showing the lowest uncertainties, i.e. lower errors and higher correlations (see Fig. 6, lower row). During all analyses, ICOS  
330 shows generally the highest uncertainties. Potential explanation is the discrepancy in spatial resolutions (see Tab. 1) as will be  
331 discussed in more detail in sec. 4.



332

333 Figure 6: Estimated root-mean-square-error ( $\sigma_{\epsilon}$ ) [mm/day] (on the x- and y- axes) and correlation ( $\rho_{t,x}$ ) [-] (on the arcs) among ET products  
 334 at all stations based on the extended triple collocation (ETC) method from McColl et al., (2014). Numbers represent the eight stations and  
 335 colours the different ET products. 1<sup>st</sup> row: ETC between SEVIRI, MODIS, and GLEAM datasets respectively with ERA5-land and ICOS.  
 336 2<sup>nd</sup> row: ETC between SEVIRI, MODIS, and GLEAM datasets respectively with GLDAS-2 and ICOS.

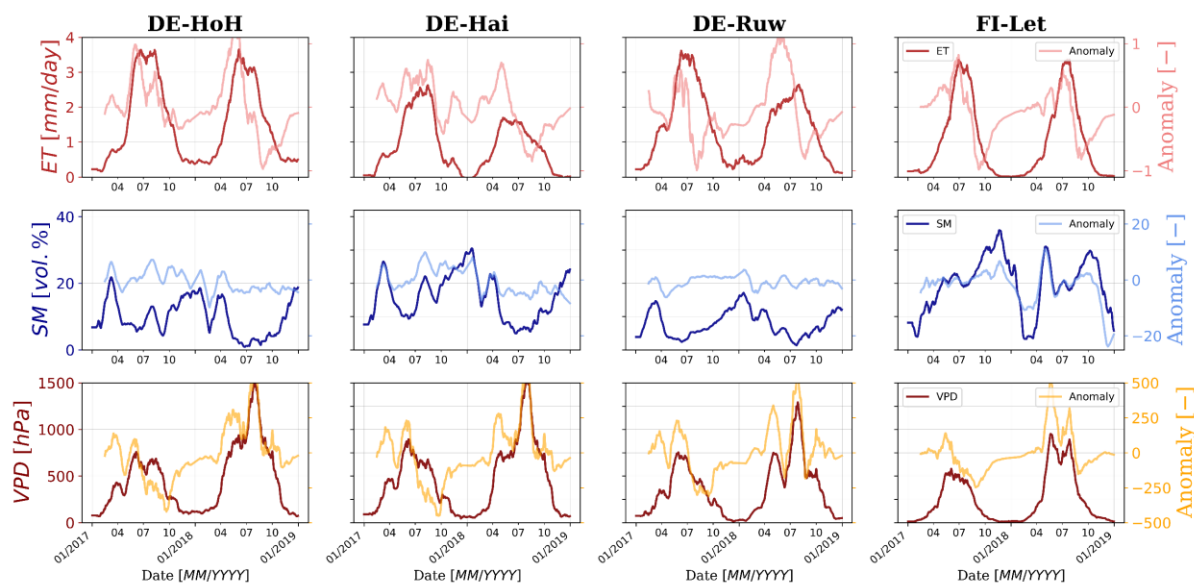
### 337 3.2 Drought impacts on ET products

338 As shown in Figures 3 and S1, 2018 was an exceptional dry year across central Europe. In this section, the impact of the  
 339 drought in 2018 on ET is investigated by comparing it to SM and VPD, the two main parameters that are used for monitoring  
 340 drought-related terrestrial ecosystem productivity (see Sec. 1). For that, we will compare 2018 always to the rather wet year  
 341 2017 to identify significant changes.

342 In Figure 7, the time series of ICOS ET, SMAP SM, and in-situ measured VPD for 2017 and 2018 are compared to their  
 343 respective calculated anomalies (see Sec. 2.3.2) for DBF (DE-HoH, DE-Hai) and ENF (DE-Ruw, FI-Let) stations. While ET  
 344 and VPD show a distinct seasonal pattern at all stations with highest values during summer months, SM shows a less clear  
 345 seasonal pattern with more inter- and intra-annual variations. At both DBF stations and the ENF station DE-Ruw, the highest  
 346 SM values are generally found during the winter months. In contrast, at ENF station FI-Let, an almost constantly increasing  
 347 SM in 2017 can be observed with a distinct drop from in January 2018 and subsequent distinct increase in April 2018. The SM  
 348 also stays at high values throughout the entire summer until mid of October in 2018, besides a smaller decrease from end of



349 May until August. However, these SM values may be an artefact of snow cover or frozen ground at the northernmost station  
350 and should be treated carefully, although the MT-DCA is quality controlled and filtered for that (see Sec. 2.2).



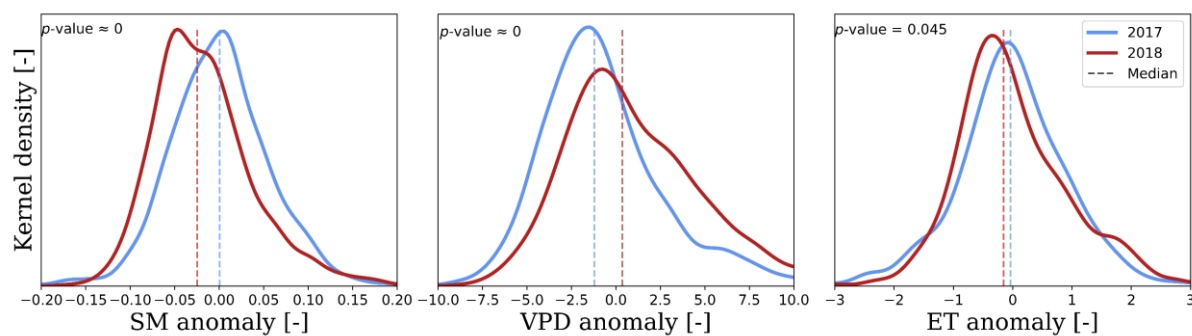
351 Figure 7: Time series of daily ICOS ET [mm/day], SMAP SM [vol.%], and in-situ VPD [hPa] for 2017 and 2018 at DBF (DE-HoH, DE-  
352 Hai), and ENF (DE-Ruw, FI-Let) stations compared to their respective anomalies (see Sec. 2.3.2). All time series were cleaned for daily and  
353 weekly dynamics using a Savitzky-Golay (Savitzky and Golay, 1964) filter with a window size of 31 days.

354 From these time series, in general lower ET and higher VPD values can be found in 2018 compared to 2017, reflecting the  
355 drought conditions with higher atmospheric aridity and decreased water supply for plant transpiration and soil evaporation in  
356 2018. At the MF (CZ-Lnz, CH-Lae) and agriculture (DE-Rus, FR-Bil) stations, the same trends can be observed but with minor  
357 differences in VPD maxima between 2017 and 2018, and sometimes higher ET peaks in 2018 at stations CZ-Lnz and FR-Bil  
358 (see Fig. S9). The overall lowest SM values can also be found in 2018, except at station FI-Let. At the DBF stations and station  
359 DE-Ruw, constantly low SM values over several months from mid of April to mid of October are shown without any significant  
360 increase during this time in 2018 (see Fig. 7). The same is true at MF station CH-Lae and the agricultural stations. At station  
361 CZ-Lnz, SM is varying monthly at low values between ~5 vol.% and 18.6 vol.% (see Fig. S9). When analysing the anomaly  
362 time series (seasonal detrending; see Sec. 2.3.2) of each parameter and station, in general higher ET and VPD anomalies and  
363 lower SM anomalies are found in 2018 compared to 2017, except at station FI-Let with higher SM anomalies in 2018 compared  
364 to 2017 (see Figs. 7 & S9).

365 These anomalies are subsequently used in Figure 8 to visualize the kernel densities of SM, VPD, and ET anomalies of all  
366 stations for 2017 and 2018. In Figure 8, only the vegetation periods from April to October within each year are analysed. It  
367 can be seen that in 2018 (drought year), the SM and ET anomalies peak at lower, negative values compared to 2017, where  
368 they peak around zero, while the VPD anomalies peak at higher, positive values compared to 2017. Also, the respective



369 anomaly medians are lower for SM and ET, and higher for VPD in 2018. The calculated  $p$ -values of always  $\leq 0.045$  prove the  
370 shift in yearly median values at the 5 % significance level.

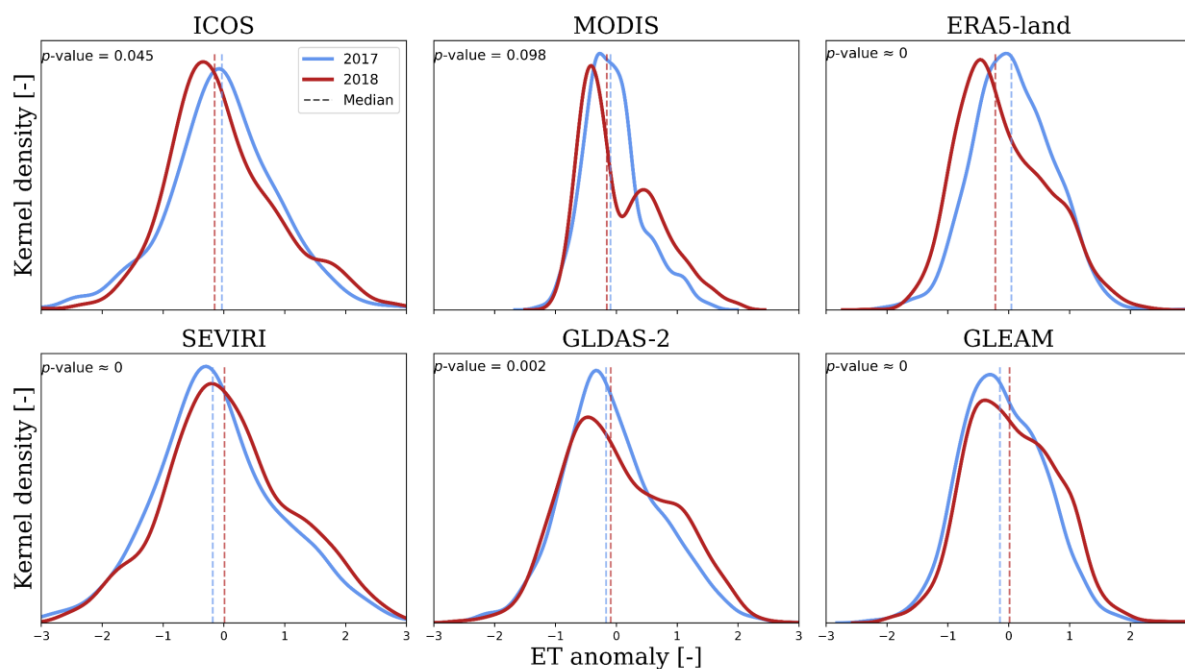


371  
372 Figure 8: Kernel density estimates of daily SMAP SM, in-situ VPD, and ICOS ET anomalies (see Sec. 2.3.2) during April to October of  
373 2017 and 2018 across all investigated stations. The dashed lines represent the seasonal median of respective parameters and years. The  $p$ -  
374 values of a two-sided Wilcoxon rank-sum test indicate the acceptance ( $> 0.05$ ) or rejection ( $< 0.05$ ) of the null hypothesis regarding  
375 continuous distributions with equal medians at the 5 % significance level.

376 When comparing the anomalies for different ET products (see Fig. 9), a similar shift towards lower values for 2018 compared  
377 to 2017 can be found for MODIS and ERA5-land products. For SEVIRI, GLDAS-2, and GLEAM a shift towards higher  
378 anomalies in 2018 is found with medians at slightly higher values compared to 2017. However, while the ICOS  $p$ -value of  
379 0.045 being close to the 5 % significance level of equal medians, the ones of SEVIRI, GLDAS-2 and GLEAM are more  
380 significant around zero. GLEAM anomalies peak at the same value for both years but with higher positive anomalies for 2018  
381 at values greater than 0.6. In general, Gaussian distributions around zero are evident for both years at all anomalies of ET  
382 products. Only at MODIS, a clear bimodal distribution in ET anomalies of 2018 with a first peak around -0.4 and a subsequent  
383 second smaller peak at 0.55 can be found. This is also the ET product with the smallest anomaly range from -1.5 to 2.5. All  
384 other ET products vary at least between -3 and 3. For the ET products ERA5-land, GLDAS-2, and GLEAM, a non-linear  
385 decrease in 2018 can be found with almost stagnating anomalies around one. For the ICOS and SEVIRI data, this trend is first  
386 visible at values greater than one. In contrast, the density curves of ET anomalies for 2017 are smoother for all products,  
387 showing a clear Gaussian distribution. Again, the calculated  $p$ -values of  $\leq 0.02$  prove the shift in yearly median values at the  
388 5 % significance level, except for the MODIS product ( $p$ -value  $< 0.1$ ). The MODIS product is also the ET product with the  
389 lowest temporal resolution of eight days (see Tab. 1). When analysing all other ET products at the same 8-daily resolution (see  
390 Fig. S10) similar bimodal distributions in 2018 can be found for ERA5-land, SEVIRI, and GLEAM. GLDAS-2 shows even a  
391 trimodal distribution with the highest density of ET anomalies around -4.5, a second peak around 1.4, and a third peak around  
392 6.3. Although no clear bimodal distribution can be seen for ICOS even at 8-daily resolution, the distribution smoothly increases  
393 from -15 to -4 and then non-linearly decreases with at least three smaller plateaus (see Fig. S10). And even for 2017, the  
394 Gaussian distributions are not that smooth as for the daily analyses. More detailed analyses revealed that there is a distinct  
395 drop in 8-daily anomaly time series, leading to this bimodal distribution. Between April and August almost only positive ET



396 anomalies are found, while during September and October almost only negative anomalies are found. The same trend is, of  
397 course, also visible for the daily time series but due to the preserved daily and intra-weekly dynamics, the difference between  
398 positive and negative anomalies during both periods (April-August, September-October) is not that distinct. These small-scale  
399 dynamics are excluded in the 8-daily analyses. However, the differences in ET anomalies between 2017 and 2018 are greater  
400 for the 8-daily anomaly analyses (see Fig. S10) compared to the daily anomaly analyses (see Fig. 9), indicating that drought  
401 impacts on ET are more pronounced at larger time scales (more than a week, monthly) than on smaller time scales (less than  
402 a week, daily). In summary, the reason for the bimodal distribution in ET anomalies within the MODIS products originates  
403 from the lower temporal resolution.



404

405 Figure 9: Kernel density estimates of daily ET anomalies (see Sec. 2.3.2) for all investigated ET products during April to October of 2017  
406 and 2018 across all investigated stations. The dashed lines represent the seasonal median of respective parameters and years. The  $p$ -values  
407 of a two-sided Wilcoxon rank-sum test indicate the acceptance ( $> 0.05$ ) or rejection ( $< 0.05$ ) of the null hypothesis regarding continuous  
408 distributions with equal medians at the 5 % significance level.

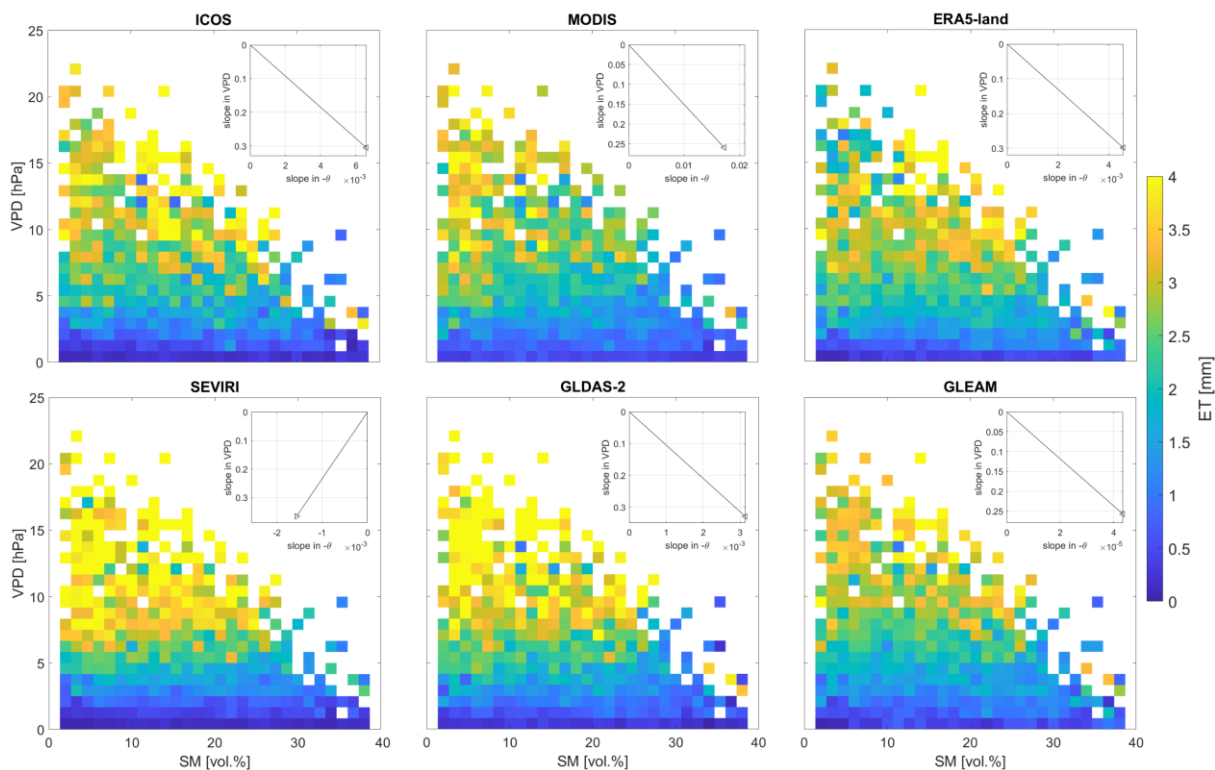
409 For analysing the dependencies between ET, SM and VPD, respective ET products in SMAP SM and in-situ measured VPD  
410 bins (see Sec. 2.3.3) are visualized for the wet year 2017 (see Fig. 10) and the dry year 2018 (see Fig. 11) across all stations.  
411 ET for all stations and both years are similarly distributed across the SM and VPD phase space.

412 For the rather wet year 2017, a general decreasing trend in ET values along increasing VPD and increasing SM can be found  
413 for all ET products except SEVIRI. Here, a decreasing trend along increasing VPD but decreasing SM is visible as indicated  
414 by the arrow within the inset plot (see Fig. 10). Overall, ET varies more with VPD than SM. Only ET from ICOS and to some





415 extend ERA5-land and GLEAM have highest values at intermediate VPD and SM, and lower ET at low SM. Especially ET  
416 products SEVIRI and GLDAS-2 do not display any reductions at low SM.



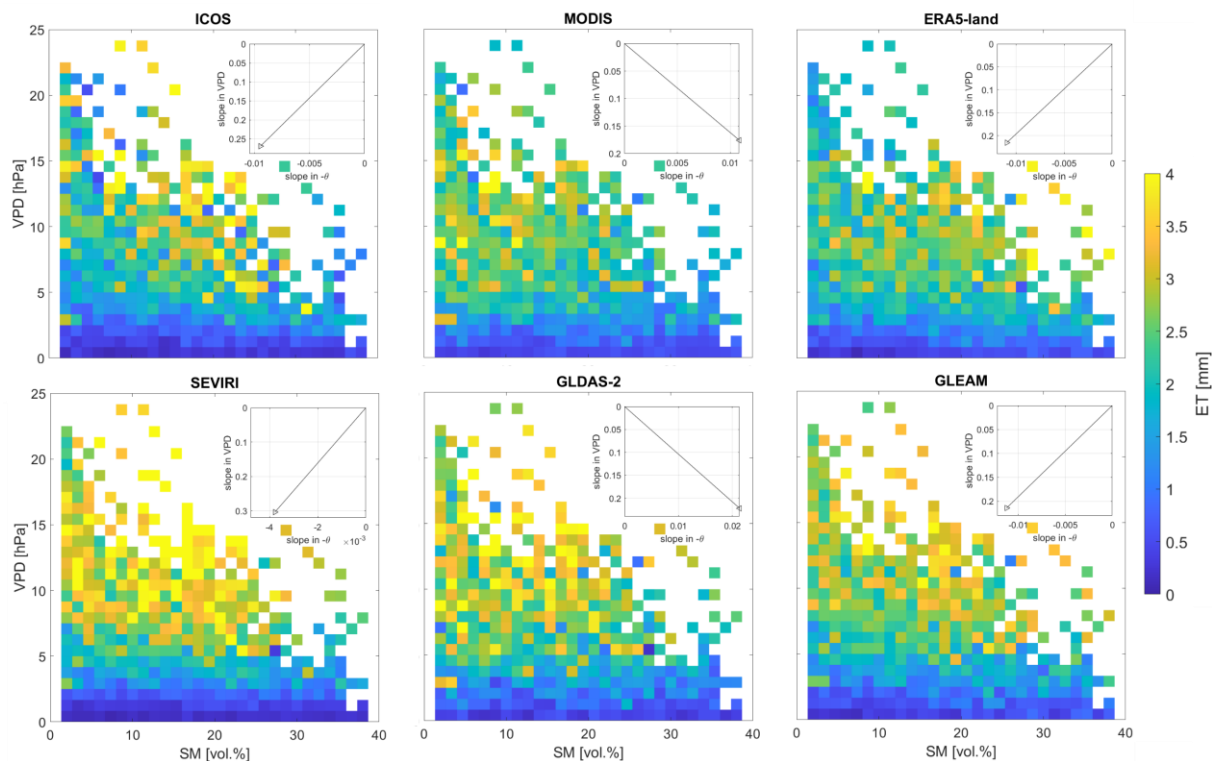
417  
418 Figure 10: ET [mm] relative to SMAP SM [vol. %] and in-situ VPD [hPa] for all investigated ET products and averaged over all investigated  
419 ICOS stations in 2017. The inset plots provide the corresponding median slope in SM and VPD changes.

420 For the dry year 2018, only MODIS and GLDAS-2 still show a decreasing trend along increasing VPD for increasing SM. All  
421 other products indicate decreasing ET for increasing VPD and decreasing SM (see. Fig. 11). At SEVIRI, the slope in SM  
422 direction is twice as low in 2018 compared to 2017 but almost the same for VPD, meaning greater decrease in ET along SM  
423 during the dry year. A similar trend is observable at MODIS with half of the slope along SM in 2018 compared to 2017,  
424 meaning half as strong increase in ET values with SM during the drought affected year 2018. Lastly, at GLDAS-2, the slope  
425 along SM bins is increased by a factor of almost seven in addition to a reduced slope in VPD of  $\sim 0.1$  hPa in 2018, meaning  
426 stronger increase in ET values at increasing SM at simultaneously decreasing VPD during the drought year. Further, ET values  
427 are in general lower in 2018 compared to 2017, but in 2018, bins at higher VPD values with low ET can be found across the  
428 entire SM range (see Fig. 11).

429 In summary, for both years, ET is generally higher at high VPD, i.e., higher atmospheric water demand, and much lower below  
430 a VPD of 5 hPa. In figures 10 and 11, we do not really see very clear reductions of ET with decreasing SM. Hence, ET varies



431 more with VPD than SM. The influence of SM on ET is only noticeable when comparing the wet (2017) and dry (2018) years  
432 with each other, as the change along SM ( $\frac{\Delta ET}{\Delta SM}$ ) is significantly higher during the drought affected year.



433

434 Figure 11: ET [mm] relative to SMAP SM [vol. %] and in-situ VPD [hPa] for all investigated ET products and averaged over all investigated  
435 ICOS stations in 2018. The inset plots provide the corresponding median slope in SM and VPD changes.

436



## 437 4 Discussion

### 438 4.1 Differences in examined ET products

439 When evaluating the performance of all ET products from remote sensing, reanalysis, modelling and ground-based eddy  
440 covariance measurements, analyses of their time series revealed that the ICOS ET almost always show a time lag of about few  
441 weeks during spring ET rise compared to all other products (see Fig. 4). This could be explained by the discrepancy in spatial  
442 resolutions, with the ICOS product providing local point-scale measurements compared to the other larger-scale remote sensing  
443 and modelling ET products. This spatial mismatch alters the vegetation impact within the ET signal. Another reason is the  
444 dependency of models on indicators for phenological changes in vegetation. For example, many models use the leaf-area index  
445 (LAI) to track phenology dynamics, which influence ET simulations (Adeluyi et al., 2021). Further, the overall lowest ET  
446 values were found for all products at the agricultural station DE-Rus, while highest values were found at the southernmost  
447 station FR-Bil, where the highest average precipitation was recorded between 2017 to 2020 (see Fig. 3). Reason for that are  
448 for one, reduced transpiration of agricultural sites throughout the year compared to forested sites, and second, the humid  
449 Atlantic climate at the southernmost station. The 8-day analyses showed that MODIS gives higher values compared to all other  
450 ET products at two stations, while ICOS is higher than all other ET products at one station. Further, the highest density of  
451 values was found between 0 to 10 mm/8-days due to the seasonal imprint with reduced ET across Europe during months with  
452 reduced solar radiation and vegetation cover (November-March). Only at the two coniferous forest stations (DE-Ruw, FR-  
453 Bil), the highest density of values is between 0 to 20 mm/8-days with lower ET values only during winter months (December-  
454 February). However, this does not apply to the third coniferous station FI-Let, which is the northernmost station with less  
455 dense forests and more snow fall between November and March, which influences the estimation of ET. Hence, the lack of  
456 leave-off conditions and the reduced amount of days with snow cover influences the amount of ET. Conducted statistics  
457 confirmed the noticeable differences among ET products and ICOS stations, which indicated an overall lower agreement  
458 among products at the rather mixed agricultural station (DE-Rus) and better consistency at ENF stations (DE-Ruw, FI-Let).  
459 Hence, products differ most at stations with complex land cover conditions, where varying crops and growing seasons  
460 (changing phenology) make the estimation of ET more difficult, while evergreen needle-leaved stations with less changes  
461 throughout the year and between years are easier to define (temporal homogeneity).

462 For more detailed product performance analyses, the extended triple collocation (ETC) method (McColl et al., 2014) revealed  
463 highest uncertainties for the ICOS product, and lowest uncertainties for SEVIRI and GLEAM as well as ERA5-land. The  
464 highest error was estimated for GLDAS-2, when analysing with GLEAM and ICOS, while the lowest sensitivity (correlation)  
465 was found for ICOS, when analysing with GLDAS-2 and MODIS (see Sec. 4.1). Hence, the remote sensing products (SEVIRI,  
466 GLEAM) and the reanalysis product (ERA5-land) differed most from the in-situ field-scale (ICOS) and modelling (GLDAS-  
467 2) products. One reason for the mismatch between the ICOS product and SEVIRI, GLEAM and ERA5-land is surely the spatial  
468 mismatch between the point-scale ground-based EC tower measurements and the remote sensing (3 km) or reanalysis (9 km)  
469 products. However, in order to capture vegetation stress, ecosystem health, and fine-scale variability in ET globally, adequate



470 spatial (and temporal) resolutions are necessary. Further, ET measurements based on the eddy covariance method tend to  
471 underestimate sensible heat (H) and latent heat (LE) fluxes (Petropoulos et al., 2015), are often temporally too short and  
472 spatially too sparse to sample drought conditions correctly (Zhao et al., 2022), and suffer from challenges to close the energy  
473 balance (Yu et al., 2023). Several studies (Twine et al., 2000; Petropoulos et al., 2015; Barrios et al., 2024) reported an error  
474 range of EC measurements of ~10-30 % due to, e.g., a ‘systematic closure problem in the surface energy budget’ (Twine et  
475 al., 2000). In order to identify potential product dependencies, which may impact the ETC results, the estimated error cross-  
476 correlations (ECC) were calculated, with high ECC between GLDAS-2 and GLEAM (at DE-HoH), between ERA5-land and  
477 GLEAM (at CZ-Lnz), and all products and GLEAM (at DE-Rus). These need to be accounted for when analysing the  
478 differences among ET products. Although in this study, we have analysed different land cover classes within a 3 km footprint  
479 around every ICOS station at daily resolution to account for the different resolutions, the SEVIRI product provides ET data  
480 every 30 minutes at moderate spatial resolution (3 km), and showed to capture ET dynamics on small as well larger temporal  
481 scales comparable or even better than other examined products, as also reported by previous studies, e.g., (Hu et al., 2015;  
482 Petropoulos et al., 2015; De Santis et al., 2022). None of the other examined products can provide similar spatio-temporal  
483 coverage, due to either lower temporal resolution (MODIS) or coarser spatial resolution (ERA5-land, GLDAS-2, GLEAM).  
484 Only the ICOS data provide similar temporal resolution to SEVIRI but at point-scale, which disqualifies it for global analyses.  
485 Although there exist other ET products from remote sensing and modelling, e.g., (Jiménez et al., 2011; Mueller et al., 2013;  
486 Fisher et al., 2020; De Santis et al., 2022; Yu et al., 2023), the examined ET products in this study are appropriate when  
487 addressing global analyses since other products have either a more coarse spatial or temporal resolution (Yu et al., 2023), or  
488 are limited to clear sky conditions (De Santis et al., 2022), which prohibits continuous time series of ET measurements. We  
489 also analysed data from the ECOSystem Spaceborne Thermal Radiometer Experiment on Space Station (ECOSTRESS)  
490 launched by NASA in June 2018 (Fisher et al., 2020) at the beginning of our analyses. However, we found several problems  
491 with this product and worse performance compared to other ET products, meaning a clear overestimation using the  
492 ECO3ETPTJPL product, as reported also by previous studies, e.g., (Liu et al., 2021; De Santis et al., 2022; Wu et al., 2022).  
493 In our research with ECOSTRESS, data was unavailable at CZ-Lnz and FI-Let. Another ECOSTRESS ET product, the  
494 ECO3ETALEX (based on the DisALEXI model), has shown better performance, but it is more suited for agricultural  
495 applications, and it is limited to the United States (Cawse-Nicholson and Anderson, 2021). ECOSTRESS level 3 ET data come  
496 at the advantage of a high spatial resolution (70 m), but its temporal resolution is irregular due to the ISS orbit and the  
497 dependency on the product type and study region limited our preliminary analyses. For these reasons, we decided not to include  
498 it in our research.

#### 499 **4.2 Impact of droughts on ET products**

500 Since remote sensing-based ET products are not purely observational, the performance of an ET product is highly dependent  
501 on the employed retrieval model for ET estimation. This is in turn dependent on how the model deals with limitations in SM  
502 or VPD and responses under drought conditions. Many studies reported decreasing ET during droughts due to reduced SM



503 supply and hence, decreasing evaporation, but also decreasing transpiration since plants close their stomata to prevent water  
504 loss (Novick et al., 2016; Zhao et al., 2022). However, during drought conditions with increasing air temperatures, ET can also  
505 increase due to the higher atmospheric moisture demand (increasing VPD). Further, the generic statement that ET decreases  
506 due to decreasing SM often ignores the fact that plants have access to SM from greater soil depths, which are not immediately  
507 affected by meteorological droughts, or have different strategies for drought resistance (Gupta et al., 2020; Feldman et al.,  
508 2024). Hence, the dynamics of ET to drought conditions remain highly variable (Zhao et al., 2022). Novick et al., (2016)  
509 pointed out that SM and VPD may become more decoupled in the future and models need to resolve limitations in SM and  
510 VPD independently from each other in order to capture the response of ecosystems to water stress correctly (Novick et al.,  
511 2016; Zhao et al., 2022). How models react to limitations in SM and VPD varies significantly which impacts resulting ET.  
512 Analyses performed in this study revealed that during the rather wet year 2017, ET varied more with VPD than with SM, with  
513 almost no dependency of ET on SM in SEVIRI and GLDAS-2 products. Here, our results indicate that ET is more controlled  
514 by atmospheric demand rather than atmospheric supply as reported also by Zhou et al., (2019). However, it is suggested by  
515 previous work and the Budyko framework (Budyko and Miller, 1974) that ET should exhibit some level of dependence on SM  
516 (Porporato et al., 2002; Zhang et al., 2021). One reason could be that forests at selected ICOS stations might have substantial  
517 access to deeper SM (root zone) that exceeds the measurement depths of the SMAP satellite (first 25 cm) (Feldman et al.,  
518 2022). When analysing the controls of SM and VPD on ET during the dry year 2018 however, all ET products, except MODIS  
519 and GLDAS-2, showed that ET decreases with increasing VPD and decreasing SM. For SEVIRI, even a twice as large decrease  
520 in ET along SM during the drought year could be observed compared to the rather wet year. This declining trend of ET during  
521 dry years when ET is limited by moisture and VPD is increasing due to increasing air temperatures is in line with previous  
522 studies (Jung et al., 2010; Seneviratne et al., 2010; Zhou et al., 2019). Further, results show that VPD and SM are negatively  
523 coupled during extreme events as reported also by (Zhou et al., 2019). However, MODIS and GLDAS-2 products showed an  
524 increase of ET with increasing SM and with decreasing VPD during 2018 (see Fig. 11). These are the two products that are  
525 based on the Penman-Monteith equation (see Tab. 1), and that were outperformed by SEVIRI, ERA5-land and GLEAM in the  
526 ETC analyses (see Fig. 6). For MODIS, one reason for the worse performance was found to be the coarse temporal resolution  
527 of 8-days, since at this time scale the temporal variability of ET is significantly different lacking all diurnal and day-to-day ET  
528 dynamics. The underperformance of MODIS compared to in-situ EC measurements was also reported by (De Santis et al.,  
529 2022), who found that MODIS overestimated in-situ ET measurements at stations in Italy, as well as (Yu et al., 2023), who  
530 investigated several stations with different land covers and varying climatic zones across the U.S. They concluded that daily  
531 or monthly ET products performed best compared to EC tower measurements (Yu et al., 2023). Due to the temporal resolution,  
532 MODIS is the only product showing a bimodal distribution of ET anomalies with a *p*-value above the 5 % significance level  
533 (see Fig. 9). In this study, we could show that differences in ET anomalies between 2017 and 2018 are greater for the 8-daily  
534 anomaly analyses (see Fig. S10) compared to the daily anomaly analyses (see Fig. 9), indicating that drought impacts on ET  
535 are more pronounced at larger time scales (more than a week, monthly) than on smaller time scales (daily, less than a week).





536 Hence, the temporal scale for ET analyses is crucial in order to select which temporal component of the ET dynamics should  
537 be considered for a respective application.

538 Further, although GLEAM is built on the less parameterized Priestly-Taylor equation compared to the Penman-Monteith  
539 equation since it does not consider VPD or canopy conductance on soil water stress, the GLEAM ET product showed to deliver  
540 better ETC results and statistics in this study. A comparable or even better performance of the Priestley-Taylor equation  
541 compared to the Penman-Monteith was also reported in previous studies, e.g., (Akumaga and Alderman, 2019; Bottazzi et al.,  
542 2021). Reasons could be the uncertainties of input variables within the Penman-Monteith equation, e.g., for stomatal or canopy  
543 resistance, which are often unknown, approximated (Widmoser, 2009), or parameterized based on the wrong variable (Hu et  
544 al., 2015), or due to the overestimation of specific parameters, such as the net radiation, or other aerodynamic factors as  
545 reported by (Hao et al., 2018). Similar, Hu et al., (2015) stated that MODIS tends to overestimate water stress during thawing  
546 of frozen soil in Spring or over irrigated land, which leads to an underestimation of soil evaporation. Moreover, several studies  
547 pointed out that the Penman-Monteith equation needs to be adapted for climate/weather extremes and vegetation limited cases,  
548 e.g., (Widmoser, 2009; Hao et al., 2018; McColl, 2020).

## 549 **5 Conclusion and Outlook**

550 In this study, eight different ET products with varying temporal and spatial resolutions as well as varying ET retrieval methods  
551 are analysed across central Europe for the period of 2017 to 2020. Despite the spatial mismatch (in-situ vs. remote sensing)  
552 and the spatial heterogeneity of the analysed landscapes (see Fig. 2), all products showed a concurrent seasonal pattern and  
553 overall low uncertainties during ETC analyses. It was shown that ET varied from year to year for different forest and  
554 agricultural stations due to changing seasonal weather and vegetation conditions over the years. Analyses revealed that  
555 temporal and spatial homogeneity helps with the consistency and interpretability of the ET estimates. This is, products were  
556 most consistent with each other at stations with less complex land cover conditions and changes throughout the seasons (the  
557 evergreen needle-leaved stations DE-Ruw and FI-Let). Despite the good match in seasonal patterns, differences in ET products  
558 were noticeable. The remote sensing products, SEVIRI, MODIS, and GLEAM, performed equivalently well or even better  
559 than the in-situ measured (ICOS), modelled (GLDAS-2) or reanalysis (ERA5-land) products. Extended triple collocation  
560 (ETC) and SM-VPD binned ET analyses revealed that SEVIRI and ERA5-land (the two products based on the (H-) Tessel  
561 land surface scheme) perform best. They provide low uncertainties when compared with other products and reasonable SM  
562 and VPD controls on absolute ET. GLEAM also shows a good performance, although this result should be taken with caution  
563 since potential product dependencies with ERA5-land and GLDAS-2 may have affected the ETC results. When analysing the  
564 behaviour of ET in context of SM and VPD during the rather wet year 2017 and dry year 2018, it was found that in 2017, ET  
565 is highly dependent on VPD and less on SM. Hence, with sufficient moisture supply, ET is mainly controlled by atmospheric  
566 demand and the vegetation transpiration. In contrast, in 2018, limited moisture supply because of decreasing SM and increasing  
567 VPD, which were in turn due to increasing air temperatures, led to a decline in ET, in line with previous studies. Further,



568 during the dry year 2018, SM and VPD were more negatively coupled which could also had an impact on the ET decline.  
569 These behaviours were consistently found in all ET products, except for GLDAS-2 and MODIS, the two products whose  
570 retrieval approaches are based on the Penman-Monteith equation. Hence, although GLEAM is based on the less parameterized  
571 Priestley-Taylor equation compared to the Penman-Monteith equation, it is outperforming GLDAS-2 and MODIS within this  
572 study set-up, which supports the idea to adapt the Penman-Monteith equation as reported by previous studies, e.g., (Widmoser,  
573 2009; Hao et al., 2018; Akumaga and Alderman, 2019; McColl, 2020; Bottazzi et al., 2021). In summary, when considering  
574 all conducted analyses together (spatial and temporal resolutions, product dependencies, ETC results, SM and VPD controls  
575 on ET), the remote sensing products SEVIRI and GLEAM as well as reanalysis product ERA5-land seems to provide most  
576 reasonable results compared all other ET products, with SEVIRI providing a higher temporal and spatial resolution compared  
577 to GLEAM and ERA5-land.

578 This study served as a pathfinder to compare freely available ET products at highly monitored EC towers across central Europe.  
579 Whether these reported findings hold true across space and for other drought events has to be analysed further with focus on  
580 spatially larger regions and longer time series. Additionally, potential add-on studies could include the examination and  
581 comparison of ET dynamics from optical/thermal remote sensing observations with microwave remote sensing data, e.g. the  
582 Sentinel-1 backscatter, in order to evaluate the potential of active microwave remote sensing for drought monitoring, e.g.,  
583 (Mueller et al., 2022; Jagdhuber et al., 2023). In order to identify relevant conditions and causal strengths with lagged and  
584 contemporaneous causal dependencies between different variables, like ET, the Sentinel-1 backscatter and other important  
585 SPAS parameters, like air temperature, relative humidity, and water potentials, the use of emerging powerful tools for causal  
586 discovery could prove useful (Runge et al., 2019; Díaz et al., 2022). Previous studies already outlined the potential of  
587 identifying causal relations between Earth system parameters (i.e., precipitation, ET, SM, air temperature) by using the wavelet  
588 coherency analysis (WCA) (Graf et al., 2014; Rahmati et al., 2020), or the PC algorithm Momentary Conditional Independence  
589 (PCMCI) method (Runge et al., 2019, 2023).

590

591

#### 592 *Data availability.*

593 The SMAP MT-DCA V5 soil moisture dataset is available at <https://zenodo.org/records/5619583>, last access: 11 May 2022.  
594 The SPEI dataset is available at <https://spei.csic.es/database.html>, last access: 18 November 2023. The evapotranspiration  
595 products are available as follows: ICOS data are available at <https://www.icos-cp.eu/>, last access: 20 November 2023. SEVIRI  
596 data are available at <https://datalsasaf.lsasvcs.ipma.pt/PRODUCTS/MSG/MDMETv3/>, last access: 21 November 2023.  
597 MODIS data are available at <https://lpdaac.usgs.gov/products/mod16a2v061/>, last access: 20 November 2023. ERA5-land data  
598 are available at <https://cds.climate.copernicus.eu/datasets/reanalysis-era5-land?tab=overview>, last access: 20 November 2023.  
599 The GLDAS-2 data are at <https://ldas.gsfc.nasa.gov/gldas/model-output>, last access: 22 November 2023. The GLEAM data  
600 are available at <https://www.gleam.eu/>, last access: 23 August 2024. The Corine land cover classes are available at



601 <https://land.copernicus.eu/en/products/corine-land-cover/clc2018?hash=4ecde146e6ca8dd7a42f68a9f5370153d9731a95>, last  
602 access: 14 March 2024.

603

604 *Author contributions.*

605 TJ designed the study concept and assembled the research team. AF, MB, MP, BB, MR, CM, and TJ were involved in the data  
606 acquisition and in developing the methodology. AF led the data curation and visualization of results. The original draft was  
607 written and prepared by AF and TJ. Draft editing and review were done by all authors.

608

609 *Competing interests.*

610 The contact author has declared that neither they nor their co-authors have any competing interests.

611

612

613

614

615

616 *Financial support.*

617 David Chaparro was supported by ‘Fundació La Caixa’ project LCF/BQ/PI23/11970013, and by the H2020 Project  
618 FORGENIUS (Improving access to FORest GENetic resources Information and services for end-USers).

619 María Piles thanks the support of *Conselleria de Innovación, Universidades, Ciencia y Sociedad Digital* through the project  
620 AI4CS CIPROM/2021/56.

621

622

623

## 624 **References**

625 Adeluyi, O., Harris, A., Verrelst, J., Foster, T., and Clay, G. D.: Estimating the phenological dynamics of irrigated rice leaf  
626 area index using the combination of PROSAIL and Gaussian Process Regression, *International Journal of Applied Earth  
627 Observation and Geoinformation*, 102, 102454, <https://doi.org/10.1016/j.jag.2021.102454>, 2021.

628 Ahmed, K. R., Paul-Limoges, E., Rascher, U., and Damm, A.: A First Assessment of the 2018 European Drought Impact on  
629 Ecosystem Evapotranspiration, *Remote Sensing*, 13, 16, <https://doi.org/10.3390/rs13010016>, 2020.

630 Akumaga, U. and Alderman, P. D.: Comparison of Penman–Monteith and Priestley–Taylor Evapotranspiration Methods for  
631 Crop Modeling in Oklahoma, *Agronomy Journal*, 111, 1171–1180, <https://doi.org/10.2134/agronj2018.10.0694>, 2019.

632 Allen, R. G., Pereira, L. S., Raes, D., Smith, M., and others: Crop evapotranspiration-Guidelines for computing crop water  
633 requirements-FAO Irrigation and drainage paper 56, Fao, Rome, 300, D05109, 1998.



- 634 Balsamo, G., Beljaars, A., Scipal, K., Viterbo, P., van den Hurk, B., Hirschi, M., and Betts, A. K.: A Revised Hydrology for  
635 the ECMWF Model: Verification from Field Site to Terrestrial Water Storage and Impact in the Integrated Forecast System,  
636 *Journal of Hydrometeorology*, 10, 623–643, <https://doi.org/10.1175/2008JHM1068.1>, 2009.
- 637 Barrios, J. M., Arboleda, A., Dutra, E., Trigo, I., and Gellens-Meulenberghs, F.: Evapotranspiration and surface energy fluxes  
638 across Europe, Africa and Eastern South America throughout the operational life of the Meteosat second generation satellite,  
639 *Geoscience Data Journal*, gdj3.235, <https://doi.org/10.1002/gdj3.235>, 2024.
- 640 Bastos, A., Ciais, P., Friedlingstein, P., Sitch, S., Pongratz, J., Fan, L., Wigneron, J. P., Weber, U., Reichstein, M., Fu, Z.,  
641 Anthoni, P., Arneth, A., Haverd, V., Jain, A. K., Joetzjer, E., Knauer, J., Lienert, S., Loughran, T., McGuire, P. C., Tian, H.,  
642 Viovy, N., and Zaehle, S.: Direct and seasonal legacy effects of the 2018 heat wave and drought on European ecosystem  
643 productivity, *Sci. Adv.*, 6, eaba2724, <https://doi.org/10.1126/sciadv.aba2724>, 2020.
- 644 Bayat, B., Camacho, F., Nickeson, J., Cosh, M., Bolten, J., Vereecken, H., and Montzka, C.: Toward operational validation  
645 systems for global satellite-based terrestrial essential climate variables, *International Journal of Applied Earth Observation and*  
646 *Geoinformation*, 95, 102240, <https://doi.org/10.1016/j.jag.2020.102240>, 2021.
- 647 Bayat, B., Montzka, C., Graf, A., Giuliani, G., Santoro, M., and Vereecken, H.: One decade (2011–2020) of European  
648 agricultural water stress monitoring by MSG-SEVIRI: workflow implementation on the Virtual Earth Laboratory (VLab)  
649 platform, *International Journal of Digital Earth*, 15, 730–747, <https://doi.org/10.1080/17538947.2022.2061617>, 2022.
- 650 Bayat, B., Raj, R., Graf, A., Vereecken, H., and Montzka, C.: Comprehensive accuracy assessment of long-term geostationary  
651 SEVIRI-MSG evapotranspiration estimates across Europe, *Remote Sensing of Environment*, 301, 113875,  
652 <https://doi.org/10.1016/j.rse.2023.113875>, 2024.
- 653 Beaudoin, H.: GLDAS Noah Land Surface Model L4 3 hourly 0.25 x 0.25 degree, Version 2.0,  
654 <https://doi.org/10.5067/342OHQM9AK6Q>, 2019.
- 655 Beguería, S., Vicente Serrano, S. M., Reig-Gracia, F., and Latorre Garcés, B.: SPEIbase v.2.8 [Dataset]; DIGITAL.CSIC;  
656 Version 2.8, <https://doi.org/10.20350/DIGITALCSIC/15121>, 2023.
- 657 Bottazzi, M., Bancheri, M., Mobilia, M., Bertoldi, G., Longobardi, A., and Rigon, R.: Comparing Evapotranspiration Estimates  
658 from the GEOframe-Prospero Model with Penman–Monteith and Priestley–Taylor Approaches under Different Climate  
659 Conditions, *Water*, 13, 1221, <https://doi.org/10.3390/w13091221>, 2021.
- 660 Budyko, M. I. and Miller, D. H.: *Climate and life*, Academic Press, New York, 1974.
- 661 Carminati, A. and Javaux, M.: Soil Rather Than Xylem Vulnerability Controls Stomatal Response to Drought, *Trends in Plant*  
662 *Science*, 25, 868–880, <https://doi.org/10.1016/j.tplants.2020.04.003>, 2020.
- 663 Carter, E., Hain, C., Anderson, M., and Steinschneider, S.: A Water Balance–Based, Spatiotemporal Evaluation of Terrestrial  
664 Evapotranspiration Products across the Contiguous United States, *Journal of Hydrometeorology*, 19, 891–905,  
665 <https://doi.org/10.1175/JHM-D-17-0186.1>, 2018.
- 666 Cawse-Nicholson, K. and Anderson, M.: ECOSTRESS Level-3 DisALEXI-JPL Evapotranspiration (ECO3ETALEXI) User  
667 Guide., 2021.
- 668 De Santis, D., D’Amato, C., Bartkowiak, P., Azimi, S., Castelli, M., Rigon, R., and Massari, C.: Evaluation of remotely-sensed  
669 evapotranspiration datasets at different spatial and temporal scales at forest and grassland sites in Italy, in: 2022 IEEE  
670 Workshop on Metrology for Agriculture and Forestry (MetroAgriFor), 2022 IEEE International Workshop on Metrology for



- 671 Agriculture and Forestry (MetroAgriFor), Perugia, Italy, 356–361,  
672 <https://doi.org/10.1109/MetroAgriFor55389.2022.9964755>, 2022.
- 673 Díaz, E., Adsua, J. E., Martínez, Á. M., Piles, M., and Camps-Valls, G.: Inferring causal relations from observational long-  
674 term carbon and water fluxes records, *Sci Rep*, 12, 1610, <https://doi.org/10.1038/s41598-022-05377-7>, 2022.
- 675 ECMWF: IFS Documentation CY45R1 - Part IV : Physical processes, <https://doi.org/10.21957/4WHWO8JW0>, 2018.
- 676 European Environment Agency: CORINE Land Cover 2018 (raster 100 m), Europe, 6-yearly - version 2020\_20u1, May 2020  
677 (20.01), <https://doi.org/10.2909/960998C1-1870-4E82-8051-6485205EBBAC>, 2019.
- 678 Feldman, A., Konings, A., Piles, M., and Entekhabi, D.: The Multi-Temporal Dual Channel Algorithm (MT-DCA) (5),  
679 <https://doi.org/10.5281/ZENODO.5619583>, 2021.
- 680 Feldman, A., Gianotti, D., Dong, J., Akbar, R., Crow, W., McColl, K., Nippert, J., Tumber-Dávila, S. J., Holbrook, N. M.,  
681 Rockwell, F., Scott, R., Reichle, R., Chatterjee, A., Joiner, J., Poulter, B., and Entekhabi, D.: Satellites capture soil moisture  
682 dynamics deeper than a few centimeters and are relevant to plant water uptake, <https://doi.org/10.1002/essoar.10511280.1>, 6  
683 May 2022.
- 684 Feldman, A. F., Feng, X., Felton, A. J., Konings, A. G., Knapp, A. K., Biederman, J. A., and Poulter, B.: Plant responses to  
685 changing rainfall frequency and intensity, *Nat Rev Earth Environ*, 5, 276–294, <https://doi.org/10.1038/s43017-024-00534-0>,  
686 2024.
- 687 Fisher, J. B., Tu, K. P., and Baldocchi, D. D.: Global estimates of the land–atmosphere water flux based on monthly AVHRR  
688 and ISLSCP-II data, validated at 16 FLUXNET sites, *Remote Sensing of Environment*, 112, 901–919,  
689 <https://doi.org/10.1016/j.rse.2007.06.025>, 2008.
- 690 Fisher, J. B., Lee, B., Purdy, A. J., Halverson, G. H., Dohlen, M. B., Cawse-Nicholson, K., Wang, A., Anderson, R. G., Aragon,  
691 B., Arain, M. A., Baldocchi, D. D., Baker, J. M., Barral, H., Bernacchi, C. J., Bernhofer, C., Biraud, S. C., Bohrer, G., Brunsell,  
692 N., Cappelaere, B., Castro-Contreras, S., Chun, J., Conrad, B. J., Cremonese, E., Demarty, J., Desai, A. R., De Ligne, A.,  
693 Foltýnová, L., Goulden, M. L., Griffis, T. J., Grünwald, T., Johnson, M. S., Kang, M., Kelbe, D., Kowalska, N., Lim, J.,  
694 Maïnassara, I., McCabe, M. F., Missik, J. E. C., Mohanty, B. P., Moore, C. E., Morillas, L., Morrison, R., Munger, J. W.,  
695 Posse, G., Richardson, A. D., Russell, E. S., Ryu, Y., Sanchez-Azofeifa, A., Schmidt, M., Schwartz, E., Sharp, I., Šigut, L.,  
696 Tang, Y., Hulley, G., Anderson, M., Hain, C., French, A., Wood, E., and Hook, S.: ECOSTRESS: NASA’s Next Generation  
697 Mission to Measure Evapotranspiration From the International Space Station, *Water Resources Research*, 56,  
698 e2019WR026058, <https://doi.org/10.1029/2019WR026058>, 2020.
- 699 Fu, Z., Ciais, P., Prentice, I. C., Gentile, P., Makowski, D., Bastos, A., Luo, X., Green, J. K., Stoy, P. C., Yang, H., and Hajima,  
700 T.: Atmospheric dryness reduces photosynthesis along a large range of soil water deficits, *Nat Commun*, 13, 989,  
701 <https://doi.org/10.1038/s41467-022-28652-7>, 2022.
- 702 Ghilain, N., Arboleda, A., and Gellens-Meulenberghs, F.: Evapotranspiration modelling at large scale using near-real time  
703 MSG SEVIRI derived data, *Hydrol. Earth Syst. Sci.*, 15, 771–786, <https://doi.org/10.5194/hess-15-771-2011>, 2011.
- 704 Graf, A., Bogena, H. R., Drüe, C., Hardelauf, H., Pütz, T., Heinemann, G., and Vereecken, H.: Spatiotemporal relations  
705 between water budget components and soil water content in a forested tributary catchment, *Water Resources Research*, 50,  
706 4837–4857, <https://doi.org/10.1002/2013WR014516>, 2014.





- 707 Gruber, A., Su, C. -H., Crow, W. T., Zwieback, S., Dorigo, W. A., and Wagner, W.: Estimating error cross-correlations in soil  
708 moisture data sets using extended collocation analysis, *JGR Atmospheres*, 121, 1208–1219,  
709 <https://doi.org/10.1002/2015JD024027>, 2016.
- 710 Gupta, A., Rico-Medina, A., and Caño-Delgado, A. I.: The physiology of plant responses to drought, *Science*, 368, 266–269,  
711 <https://doi.org/10.1126/science.aaz7614>, 2020.
- 712 Hao, X., Zhang, S., Li, W., Duan, W., Fang, G., Zhang, Y., and Guo, B.: The Uncertainty of Penman-Monteith Method and  
713 the Energy Balance Closure Problem, *JGR Atmospheres*, 123, 7433–7443, <https://doi.org/10.1029/2018JD028371>, 2018.
- 714 Hersbach, H., Bell, B., Berrisford, P., Hirahara, S., Horányi, A., Muñoz-Sabater, J., Nicolas, J., Peubey, C., Radu, R., Schepers,  
715 D., Simmons, A., Soci, C., Abdalla, S., Abellan, X., Balsamo, G., Bechtold, P., Biavati, G., Bidlot, J., Bonavita, M., De Chiara,  
716 G., Dahlgren, P., Dee, D., Diamantakis, M., Dragani, R., Flemming, J., Forbes, R., Fuentes, M., Geer, A., Haimberger, L.,  
717 Healy, S., Hogan, R. J., Hólm, E., Janisková, M., Keeley, S., Laloyaux, P., Lopez, P., Lupu, C., Radnoti, G., de Rosnay, P.,  
718 Rozum, I., Vamborg, F., Villaume, S., and Thépaut, J.: The ERA5 global reanalysis, *Quart J Royal Meteor Soc*, 146, 1999–  
719 2049, <https://doi.org/10.1002/qj.3803>, 2020.
- 720 Hu, G., Jia, L., and Menenti, M.: Comparison of MOD16 and LSA-SAF MSG evapotranspiration products over Europe for  
721 2011, *Remote Sensing of Environment*, 156, 510–526, <https://doi.org/10.1016/j.rse.2014.10.017>, 2015.
- 722 Hu, T., Mallick, K., Hitzelberger, P., Didry, Y., Boulet, G., Szantoi, Z., Koetz, B., Alonso, I., Pascolini-Campbell, M.,  
723 Halverson, G., Cawse-Nicholson, K., Hulley, G. C., Hook, S., Bhattarai, N., Olioso, A., Roujean, J., Gamet, P., and Su, B.:  
724 Evaluating European ECOSTRESS Hub Evapotranspiration Products Across a Range of Soil-Atmospheric Aridity and Biomes  
725 Over Europe, *Water Resources Research*, 59, e2022WR034132, <https://doi.org/10.1029/2022WR034132>, 2023.
- 726 ICOS RI, Aalto, J., Aalto, P., Aaltonen, H., Aiguier, T., Akubia, J., Ala-Könni, J., Alivernini, A., Aluome, C., Andersson, T.,  
727 Arca, A., Arriga, N., Aurela, M., BRECHET, L., Baab, F., Back, J., Baltés, U., Baneschi, I., Barten, S., Baur, T., Bauters, M.,  
728 Bazot, S., Beauclair, P., Becker, N., Belelli Marchesini, L., Bergström, G., Bernhofer, C., Berveiller, D., Biermann, T.,  
729 Bignotti, L., Biron, R., Bloor, J., Bodson, B., Boeckx, P., Bogaerts, G., Bonal, D., Boon, G., Bornet, F., Bortoli, M., Bosio, I.,  
730 Brut, A., Brümmer, C., Buchmann, N., Bulonza, E., Burban, B., Buysse, P., Båth, A., Calandrelli, D., Calvet, J.-C., Canut-  
731 Rocafort, G., Carrara, A., Cavagna, M., Ceschia, E., Chabbi, A., Chan, T., Chebbi, W., Chianucci, F., Chipeaux, C., Chopin,  
732 H., Christen, A., Chrysoulakis, N., Claverie, N., Cobbe, I., Cohard, J.-M., Colosse, D., Conte, A., Corsanici, R., Coulaud, C.,  
733 Courtois, P., Coyle, M., Cremonese, E., Crill, P., Cuntz, M., Cuocolo, D., Czerný, R., DEPUYDT, J., Daelman, R., Darenová,  
734 E., Darsonville, O., De Ligne, A., De Meulder, T., De Simon, G., Decau, M.-L., Dell’Acqua, A., Delorme, J.-P., Delpierre, N.,  
735 Demoulin, L., Denou, J.-L., Di Tommasi, P., Dienstbach, L., Dignam, R., Dolfus, D., Domec, J.-C., Douxfils, B., Drösler, M.,  
736 Drüe, C., Dufrène, E., Dumont, B., Durand, B., et al.: Ecosystem final quality (L2) product in ETC-Archive format - release  
737 2024-1, <https://doi.org/10.18160/G5KZ-ZD83>, 22 May 2024.
- 738 Jagdhuber, T., Fluhrer, A., Chaparro, D., Dubois, C., Hellwig, F. M., Bayat, B., Montzka, C., Baur, M. J., Ramati, M., Kübert,  
739 A., Mueller, M. M., Schellenberg, K., Boehm, M., Jonard, F., Steele-Dunne, S., Piles, M., and Entekhabi, D.: On the Potential  
740 of Active and Passive Microwave Remote Sensing for Tracking Seasonal Dynamics of Evapotranspiration, in: *IGARSS 2023*  
741 - 2023 IEEE International Geoscience and Remote Sensing Symposium, *IGARSS 2023 - 2023 IEEE International Geoscience*  
742 and Remote Sensing Symposium, Pasadena, CA, USA, 2610–2613, <https://doi.org/10.1109/IGARSS52108.2023.10283234>,  
743 2023.
- 744 Jiménez, C., Prigent, C., Mueller, B., Seneviratne, S. I., McCabe, M. F., Wood, E. F., Rossow, W. B., Balsamo, G., Betts, A.  
745 K., Dirmeyer, P. A., Fisher, J. B., Jung, M., Kanamitsu, M., Reichle, R. H., Reichstein, M., Rodell, M., Sheffield, J., Tu, K.,  
746 and Wang, K.: Global intercomparison of 12 land surface heat flux estimates, *J. Geophys. Res.*, 116, D02102,  
747 <https://doi.org/10.1029/2010JD014545>, 2011.



- 748 Jung, M., Reichstein, M., Ciais, P., Seneviratne, S. I., Sheffield, J., Goulden, M. L., Bonan, G., Cescatti, A., Chen, J., De Jeu,  
749 R., Dolman, A. J., Eugster, W., Gerten, D., Gianelle, D., Gobron, N., Heinke, J., Kimball, J., Law, B. E., Montagnani, L., Mu,  
750 Q., Mueller, B., Oleson, K., Papale, D., Richardson, A. D., Rouspard, O., Running, S., Tomelleri, E., Viovy, N., Weber, U.,  
751 Williams, C., Wood, E., Zaehle, S., and Zhang, K.: Recent decline in the global land evapotranspiration trend due to limited  
752 moisture supply, *Nature*, 467, 951–954, <https://doi.org/10.1038/nature09396>, 2010.
- 753 Konings, A., Piles, M., Rötzer, M., McColl, K., Chang, S. K., and Entekhabi, D.: Vegetation optical depth and scattering  
754 albedo retrieval using time series of dual-polarized L-band radiometer observations, *Elsevier Remote Sensing of Environment*,  
755 172, 178–189, <https://doi.org/10.1016/j.rse.2015.11.009>, 2016.
- 756 Li, C., Yang, H., Yang, W., Liu, Z., Jia, Y., Li, S., and Yang, D.: Error characterization of global land evapotranspiration  
757 products: Collocation-based approach, *Journal of Hydrology*, 612, 128102, <https://doi.org/10.1016/j.jhydrol.2022.128102>,  
758 2022.
- 759 Liu, H., Xin, X., Su, Z., Zeng, Y., Lian, T., Li, L., Yu, S., and Zhang, H.: Intercomparison and evaluation of ten global ET  
760 products at site and basin scales, *Journal of Hydrology*, 617, <https://doi.org/10.1016/j.jhydrol.2022.128887>, 2023.
- 761 Liu, L., Gudmundsson, L., Hauser, M., Qin, D., Li, S., and Seneviratne, S. I.: Soil moisture dominates dryness stress on  
762 ecosystem production globally, *Nat Commun*, 11, 4892, <https://doi.org/10.1038/s41467-020-18631-1>, 2020.
- 763 Liu, N., Oishi, A. C., Miniati, C. F., and Bolstad, P.: An evaluation of ECOSTRESS products of a temperate montane humid  
764 forest in a complex terrain environment, *Remote Sensing of Environment*, 265, 112662,  
765 <https://doi.org/10.1016/j.rse.2021.112662>, 2021.
- 766 Loustau, D., Chipeaux, C., and ICOS Ecosystem Thematic Centre: Warm winter 2020 ecosystem eddy covariance flux product  
767 from Bilos (1.0), <https://doi.org/10.18160/MSRT-T1YA>, 2022.
- 768 Martens, B., Miralles, D. G., Lievens, H., van der Schalie, R., de Jeu, R. A. M., Fernández-Prieto, D., Beck, H. E., Dorigo, W.  
769 A., and Verhoest, N. E. C.: GLEAM v3: satellite-based land evaporation and root-zone soil moisture, *Geosci. Model Dev.*, 10,  
770 1903–1925, <https://doi.org/10.5194/gmd-10-1903-2017>, 2017.
- 771 McColl, K. A.: Practical and Theoretical Benefits of an Alternative to the Penman-Monteith Evapotranspiration Equation,  
772 *Water Resources Research*, 56, e2020WR027106, <https://doi.org/10.1029/2020WR027106>, 2020.
- 773 McColl, K. A., Vogelzang, J., Konings, A. G., Entekhabi, D., Piles, M., and Stoffelen, A.: Extended triple collocation:  
774 Estimating errors and correlation coefficients with respect to an unknown target, *Geophysical Research Letters*, 41, 6229–  
775 6236, <https://doi.org/10.1002/2014GL061322>, 2014.
- 776 Meng, X., Deng, M., Shu, L., Chen, H., Wang, S., Li, Z., Zhao, L., and Shang, L.: An evaluation of evapotranspiration products  
777 over the Tibetan Plateau, *Journal of Hydrometeorology*, <https://doi.org/10.1175/JHM-D-23-0223.1>, 2024.
- 778 Miralles, D. G., Holmes, T. R. H., De Jeu, R. A. M., Gash, J. H., Meesters, A. G. C. A., and Dolman, A. J.: Global land-surface  
779 evaporation estimated from satellite-based observations, *Hydrol. Earth Syst. Sci.*, 15, 453–469, <https://doi.org/10.5194/hess-15-453-2011>, 2011.
- 781 Monteith, J. L.: Evaporation and environment, *Symposia of the society for experimental biology*, 19, 1965.
- 782 Mueller, B., Hirschi, M., Jimenez, C., Ciais, P., Dirmeyer, P. A., Dolman, A. J., Fisher, J. B., Jung, M., Ludwig, F., Maignan,  
783 F., Miralles, D. G., McCabe, M. F., Reichstein, M., Sheffield, J., Wang, K., Wood, E. F., Zhang, Y., and Seneviratne, S. I.:



- 784 Benchmark products for land evapotranspiration: LandFlux-EVAL multi-data set synthesis, *Hydrol. Earth Syst. Sci.*, 17, 3707–  
785 3720, <https://doi.org/10.5194/hess-17-3707-2013>, 2013.
- 786 Mueller, M. M., Dubois, C., Jagdhuber, T., Hellwig, F. M., Pathe, C., Schmulius, C., and Steele-Dunne, S.: Sentinel-1  
787 Backscatter Time Series for Characterization of Evapotranspiration Dynamics over Temperate Coniferous Forests, *Remote*  
788 *Sensing*, 14, 6384, <https://doi.org/10.3390/rs14246384>, 2022.
- 789 Muñoz Sabater, J.: ERA5-Land hourly data from 1981 to present. Copernicus Climate Change Service (C3S) Climate Data  
790 Store (CDS). (Accessed on 10-08-2022), <https://doi.org/10.24381/CDS.E2161BAC>, 2019.
- 791 Novick, K. A., Ficklin, D. L., Stoy, P. C., Williams, C. A., Bohrer, G., Oishi, A. C., Papuga, S. A., Blanken, P. D., Noormets,  
792 A., Sulman, B. N., Scott, R. L., Wang, L., and Phillips, R. P.: The increasing importance of atmospheric demand for ecosystem  
793 water and carbon fluxes, *Nature Clim Change*, 6, 1023–1027, <https://doi.org/10.1038/nclimate3114>, 2016.
- 794 Penman, H. L.: Natural evaporation from open water, bare soil and grass, *Proc. R. Soc. Lond. A*, 193, 120–145,  
795 <https://doi.org/10.1098/rspa.1948.0037>, 1948.
- 796 Petropoulos, G. P., Ireland, G., Cass, A., and Srivastava, P. K.: Performance Assessment of the SEVIRI Evapotranspiration  
797 Operational Product: Results Over Diverse Mediterranean Ecosystems, *IEEE Sensors J.*, 15, 3412–3423,  
798 <https://doi.org/10.1109/JSEN.2015.2390031>, 2015.
- 799 Porporato, A., D’Odorico, P., Laio, F., Ridolfi, L., and Rodriguez-Iturbe, I.: Ecohydrology of water-controlled ecosystems,  
800 *Advances in Water Resources*, 25, 1335–1348, [https://doi.org/10.1016/S0309-1708\(02\)00058-1](https://doi.org/10.1016/S0309-1708(02)00058-1), 2002.
- 801 Priestley, C. H. B. and Taylor, R. J.: On the Assessment of Surface Heat Flux and Evaporation Using Large-Scale Parameters,  
802 *Mon. Wea. Rev.*, 100, 81–92, [https://doi.org/10.1175/1520-0493\(1972\)100<0081:OTAOSH>2.3.CO;2](https://doi.org/10.1175/1520-0493(1972)100<0081:OTAOSH>2.3.CO;2), 1972.
- 803 Rahmati, M., Groh, J., Graf, A., Pütz, T., Vanderborght, J., and Vereecken, H.: On the impact of increasing drought on the  
804 relationship between soil water content and evapotranspiration of a grassland, *Vadose Zone Journal*, 19, e20029,  
805 <https://doi.org/10.1002/vzj2.20029>, 2020.
- 806 Rahmati, M., Graf, A., Poppe Terán, C., Amelung, W., Dorigo, W., Franssen, H.-J. H., Montzka, C., Or, D., Sprenger, M.,  
807 Vanderborght, J., Verhoest, N. E. C., and Vereecken, H.: Continuous increase in evaporative demand shortened the growing  
808 season of European ecosystems in the last decade, *Commun Earth Environ*, 4, 236, [https://doi.org/10.1038/s43247-023-00890-](https://doi.org/10.1038/s43247-023-00890-7)  
809 [7](https://doi.org/10.1038/s43247-023-00890-7), 2023.
- 810 Rahmati, M., Amelung, W., Brogi, C., Dari, J., Flammini, A., Bogen, H., Brocca, L., Chen, H., Groh, J., Koster, R. D.,  
811 McColl, K. A., Montzka, C., Moradi, S., Rahi, A., Sharghi S., F., and Vereecken, H.: Soil Moisture Memory: State-Of-The-  
812 Art and the Way Forward, *Reviews of Geophysics*, 62, e2023RG000828, <https://doi.org/10.1029/2023RG000828>, 2024.
- 813 Rakovec, O., Samaniego, L., Hari, V., Markonis, Y., Moravec, V., Thober, S., Hanel, M., and Kumar, R.: The 2018–2020  
814 Multi-Year Drought Sets a New Benchmark in Europe, *Earth’s Future*, 10, e2021EF002394,  
815 <https://doi.org/10.1029/2021EF002394>, 2022.
- 816 Rebmann, C., Aubinet, M., Schmid, H., Arriga, N., Aurela, M., Burba, G., Clement, R., De Ligne, A., Fratini, G., Gielen, B.,  
817 Grace, J., Graf, A., Gross, P., Haapanala, S., Herbst, M., Hörtnagl, L., Ibrom, A., Joly, L., Kljun, N., Kolle, O., Kowalski, A.,  
818 Lindroth, A., Loustau, D., Mammarella, I., Mauder, M., Merbold, L., Metzger, S., Mölder, M., Montagnani, L., Papale, D.,  
819 Pavelka, M., Peichl, M., Roland, M., Serrano-Ortiz, P., Siebicke, L., Steinbrecher, R., Tuovinen, J.-P., Vesala, T., Wohlfahrt,  
820 G., and Franz, D.: ICOS eddy covariance flux-station site setup: a review, *International Agrophysics*, 32, 471–494,  
821 <https://doi.org/10.1515/intag-2017-0044>, 2018.



- 822 Rui, H. and Beaudoin, H.: README Document for NASA GLDAS Version 2 Data Products, NASA Goddard Earth Sciences  
823 Data and Information Services Center (GES DISC), 2022.
- 824 Runge, J., Nowack, P., Kretschmer, M., Flaxman, S., and Sejdinovic, D.: Detecting and quantifying causal associations in  
825 large nonlinear time series datasets, *Sci. Adv.*, 5, eaau4996, <https://doi.org/10.1126/sciadv.aau4996>, 2019.
- 826 Runge, J., Gerhardus, A., Varando, G., Eyring, V., and Camps-Valls, G.: Causal inference for time series, *Nat Rev Earth  
827 Environ*, 4, 487–505, <https://doi.org/10.1038/s43017-023-00431-y>, 2023.
- 828 Running, S., Mu, Q., and Zhao, M.: MOD16A2 MODIS/Terra Net Evapotranspiration 8-Day L4 Global 500m SIN Grid V006,  
829 <https://doi.org/10.5067/MODIS/MOD16A2.006>, 2017.
- 830 Running, S., Mu, Q., Zhao, M., and Moreno, A.: User’s guide MODIS global terrestrial evapotranspiration (ET) product  
831 (MOD16A2/A3 and year-end gap-filled MOD16A2GF/A3GF), MODIS Land Team 40, 2019.
- 832 Savitzky, Abraham. and Golay, M. J. E.: Smoothing and Differentiation of Data by Simplified Least Squares Procedures.,  
833 *Anal. Chem.*, 36, 1627–1639, <https://doi.org/10.1021/ac60214a047>, 1964.
- 834 Schuldt, B., Buras, A., Arend, M., Vitasse, Y., Beierkuhnlein, C., Damm, A., Gharun, M., Grams, T. E. E., Hauck, M., Hajek,  
835 P., Hartmann, H., Hiltbrunner, E., Hoch, G., Holloway-Phillips, M., Körner, C., Larysch, E., Lübke, T., Nelson, D. B.,  
836 Rammig, A., Rigling, A., Rose, L., Ruehr, N. K., Schumann, K., Weiser, F., Werner, C., Wohlgemuth, T., Zang, C. S., and  
837 Kahmen, A.: A first assessment of the impact of the extreme 2018 summer drought on Central European forests, *Basic and  
838 Applied Ecology*, 45, 86–103, <https://doi.org/10.1016/j.baae.2020.04.003>, 2020.
- 839 Seneviratne, S. I., Corti, T., Davin, E. L., Hirschi, M., Jaeger, E. B., Lehner, I., Orlowsky, B., and Teuling, A. J.: Investigating  
840 soil moisture–climate interactions in a changing climate: A review, *Earth-Science Reviews*, 99, 125–161,  
841 <https://doi.org/10.1016/j.earscirev.2010.02.004>, 2010.
- 842 Sepulcre-Canto, G., Vogt, J., Arboleda, A., and Antofie, T.: Assessment of the EUMETSAT LSA-SAF evapotranspiration  
843 product for drought monitoring in Europe, *International Journal of Applied Earth Observation and Geoinformation*, 30, 190–  
844 202, <https://doi.org/10.1016/j.jag.2014.01.021>, 2014.
- 845 Stisen, S., Soltani, M., Mendiguren, G., Langkilde, H., Garcia, M., and Koch, J.: Spatial Patterns in Actual Evapotranspiration  
846 *Climatologies for Europe*, *Remote Sensing*, 13, 2410, <https://doi.org/10.3390/rs13122410>, 2021.
- 847 Stoffelen, A.: Toward the true near-surface wind speed: Error modeling and calibration using triple collocation, *J. Geophys.  
848 Res.*, 103, 7755–7766, <https://doi.org/10.1029/97JC03180>, 1998.
- 849 Trambauer, P., Dutra, E., Maskey, S., Werner, M., Pappenberger, F., Van Beek, L. P. H., and Uhlenbrook, S.: Comparison of  
850 different evaporation estimates over the African continent, *Hydrol. Earth Syst. Sci.*, 18, 193–212, <https://doi.org/10.5194/hess-18-193-2014>, 2014.
- 852 Twine, T. E., Kustas, W. P., Norman, J. M., Cook, D. R., Houser, P. R., Meyers, T. P., Prueger, J. H., Starks, P. J., and Wesely,  
853 M. L.: Correcting eddy-covariance flux underestimates over a grassland, *Agricultural and Forest Meteorology*, 103, 279–300,  
854 [https://doi.org/10.1016/S0168-1923\(00\)00123-4](https://doi.org/10.1016/S0168-1923(00)00123-4), 2000.
- 855 Vargas Zeppetello, L. R., McColl, K. A., Bernau, J. A., Bowen, B. B., Tang, L. I., Holbrook, N. M., Gentine, P., and Huybers,  
856 P.: Apparent surface conductance sensitivity to vapour pressure deficit in the absence of plants, *Nat Water*, 1, 941–951,  
857 <https://doi.org/10.1038/s44221-023-00147-9>, 2023.



- 858 Wang, K. and Dickinson, R. E.: A review of global terrestrial evapotranspiration: Observation, modeling, climatology, and  
859 climatic variability, *Reviews of Geophysics*, 50, 2011RG000373, <https://doi.org/10.1029/2011RG000373>, 2012.
- 860 Widmoser, P.: A discussion on and alternative to the Penman–Monteith equation, *Agricultural Water Management*, 96, 711–  
861 721, <https://doi.org/10.1016/j.agwat.2008.10.003>, 2009.
- 862 Wu, J., Feng, Y., Liang, L., He, X., and Zeng, Z.: Assessing evapotranspiration observed from ECOSTRESS using flux  
863 measurements in agroecosystems, *Agricultural Water Management*, 269, 107706,  
864 <https://doi.org/10.1016/j.agwat.2022.107706>, 2022.
- 865 Xu, C., Wang, W., Hu, Y., and Liu, Y.: Evaluation of ERA5, ERA5-Land, GLDAS-2.1, and GLEAM potential  
866 evapotranspiration data over mainland China, *Journal of Hydrology: Regional Studies*, 51, 101651,  
867 <https://doi.org/10.1016/j.ejrh.2023.101651>, 2024.
- 868 Xu, T., Guo, Z., Xia, Y., Ferreira, V. G., Liu, S., Wang, K., Yao, Y., Zhang, X., and Zhao, C.: Evaluation of twelve  
869 evapotranspiration products from machine learning, remote sensing and land surface models over conterminous United States,  
870 *Journal of Hydrology*, 578, 124105, <https://doi.org/10.1016/j.jhydrol.2019.124105>, 2019.
- 871 Yu, X., Qian, L., Wang, W., Hu, X., Dong, J., Pi, Y., and Fan, K.: Comprehensive evaluation of terrestrial evapotranspiration  
872 from different models under extreme condition over conterminous United States, *Agricultural Water Management*, 289,  
873 108555, <https://doi.org/10.1016/j.agwat.2023.108555>, 2023.
- 874 Zhang, J., Guan, K., Peng, B., Pan, M., Zhou, W., Jiang, C., Kimm, H., Franz, T. E., Grant, R. F., Yang, Y., Rudnick, D. R.,  
875 Heeren, D. M., Suyker, A. E., Bauerle, W. L., and Miner, G. L.: Sustainable irrigation based on co-regulation of soil water  
876 supply and atmospheric evaporative demand, *Nat Commun*, 12, 5549, <https://doi.org/10.1038/s41467-021-25254-7>, 2021.
- 877 Zhang, K., Kimball, J. S., and Running, S. W.: A review of remote sensing based actual evapotranspiration estimation, *WIREs*  
878 *Water*, 3, 834–853, <https://doi.org/10.1002/wat2.1168>, 2016.
- 879 Zhao, M., A. G., Liu, Y., and Konings, A. G.: Evapotranspiration frequently increases during droughts, *Nat. Clim. Chang.*, 12,  
880 1024–1030, <https://doi.org/10.1038/s41558-022-01505-3>, 2022.
- 881 Zhou, S., Yu, B., Zhang, Y., Huang, Y., and Wang, G.: Partitioning evapotranspiration based on the concept of underlying  
882 water use efficiency, *Water Resources Research*, 52, 1160–1175, <https://doi.org/10.1002/2015WR017766>, 2016.
- 883 Zhou, S., Zhang, Y., Park Williams, A., and Gentine, P.: Projected increases in intensity, frequency, and terrestrial carbon  
884 costs of compound drought and aridity events, *Sci. Adv.*, 5, eaau5740, <https://doi.org/10.1126/sciadv.aau5740>, 2019.
- 885